PROCEEDINGS A

royalsocietypublishing.org/journal/rspa

Research

Cite this article: Vilacís B, Hayek JN, Stotz IL, Bunge H-P, Friedrich AM, Carena S, Clark S. 2022 Evidence for active upper mantle flow in the Atlantic and Indo-Australian realms since the Upper Jurassic from hiatus maps and spreading rate changes. *Proc. R. Soc. A* **478**: 20210764.
https://doi.org/10.1098/rspa.2021.0764

Received: 1 October 2021
Accepted: 12 May 2022

Subject Areas:
geophysics, geology

Keywords:
dynamic topography, hiatus, oceanic spreading rates, Poiseuille flow, mantle convection, global geodynamics

Author for correspondence:
Berta Vilacís
e-mail: bvilacis@geophysik.uni-muenchen.de

THE ROYAL SOCIETY
PUBLISHING

Evidence for active upper mantle flow in the Atlantic and Indo-Australian realms since the Upper Jurassic from hiatus maps and spreading rate changes

Berta Vilacís[1], Jorge N. Hayek[1], Ingo L. Stotz[1], Hans-Peter Bunge[1], Anke M. Friedrich[1], Sara Carena[1] and Stuart Clark[2]

[1]Department of Earth and Environmental Sciences, Ludwig-Maximilians-Universität München, Theresienstraße 41 and Luisenstraße 37, Munich 80333 Germany
[2]University of New South Wales Sydney, Minerals and Energy Res. Eng., Kensington, New South Wales 2052, Australia

BV, 0000-0001-5597-2606; JNH, 0000-0002-0351-3368

Histories of large-scale horizontal and vertical lithosphere motion hold important information on mantle convection. Here, we compare continent-scale hiatus maps as a proxy for mantle flow induced dynamic topography and plate motion variations in the Atlantic and Indo-Australian realms since the Upper Jurassic, finding they frequently correlate, except when plate boundary forces may play a significant role. This correlation agrees with descriptions of asthenosphere flow beneath tectonic plates in terms of Poiseuille/Couette flow, as it explicitly relates plate motion changes, induced by evolving basal shear forces, to non-isostatic vertical motion of the lithosphere. Our analysis reveals a timescale, on the order of a geological series, between the occurrence of continent-scale hiatus and plate motion changes. This is consistent with the presence of a weak upper mantle. It also shows a spatial scale for interregional hiatus, on the order of 2000–3000 km in diameter, which can be linked by fluid dynamic analysis to active upper mantle

flow regions. Our results suggest future studies should pursue large-scale horizontal and vertical lithosphere motion in combination, to track the expressions of past mantle flow. Such studies would provide powerful constraints for adjoint-based geodynamic inverse models of past mantle convection.

1. Introduction

An enduring theme in mantle flow studies is the existence of an asthenosphere (see [1] for a review). The presence of this layer was advocated by Barrell [2] to allow for isostatic movement, and by Chase [3] to lubricate plate motion. Modern evidence for a mechanically weak layer in the uppermost mantle beneath the lithosphere comes from a variety of observations. They include studies of the geoid (e.g. [4]), post-glacial rebound (e.g. [5]), lake loading (e.g. [6]), oceanic intraplate seismicity [7], ocean ridge bathymetry [8] and seismic anisotropy [9,10]. Fluid dynamic investigations employing numerical and analytic modelling techniques (e.g. [11–13]) agree that high material mobility in the asthenosphere is essential to promote the long-wavelength character of mantle flow observed on Earth. Three-dimensional spherical Earth models that combine an asthenosphere and a plastic yield stress to allow localized weakening of the cold upper thermal boundary layer result in a distinctly plate tectonic style of convection [14].

Morgan and colleagues [15,16] linked the asthenosphere to mantle plumes, proposing an asthenosphere fed actively by hot upwellings. This and their subsequent work [17,18] explored the resulting upper mantle flow in terms of a simple model, where material flux is driven horizontally by lateral pressure variations, in order to explain various observations related to ocean bathymetry, heat flow and mantle geochemistry. A series of papers by Höink *et al.* [19–22] extended this approach. They formulated mantle convection models explicitly in the context of so-called Poiseuille/Couette flow (figure 1). An important finding is that lateral pressure variations in the asthenosphere are not tied exclusively to the influx of plume material, but occur also for convection heated purely from within. Poiseuille/Couette flow is thus an intrinsic property of material flowing in a low viscosity asthenosphere channel beneath mobile tectonic plates.

Asthenosphere flow driven by high- and low-pressure regions is a powerful concept, because it connects mantle flow to geologic observations in a testable manner. In particular, it explicitly relates temporal changes in horizontal plate motion, i.e. oceanic spreading rate variations driven by evolving basal shear stresses, to non-isostatic vertical motion of the lithosphere. The latter is a form of topography maintained dynamically by mantle convection. It was termed 'dynamic topography' by Hager *et al.* [23] more than 30 years ago (see [24] for a review).

Current plate motions are well mapped [25]. But histories of plate motion are becoming better known. Initially documented for the Cenozoic [26], global plate motion reconstructions are now available for times going back to the Mesozoic (see [27] for a review). Progress is also underway in mapping the magnetization of some ocean floor regions in great detail, permitting plate motion reconstructions at temporal resolutions of ∼1 million years (Myrs) or less (e.g. [28,29]) when mitigating for finite-rotation noise [30]. These efforts reveal that it often takes but a few Myrs for plates to change their motions. The variations may be due to changes in plate boundary forces [31] and/or basal shear stresses [32]. They provide important observations for geodynamic interpretations (see [33] for a review).

Less is known about current dynamic topography, at least outside the oceanic realm [34]. Dynamic topography for continents is difficult to map, because one needs to separate it from topography in isostatic support [35,36]. But histories of dynamic topography in the continents are beginning to emerge, because the transient nature of dynamic topography leaves geologic evidence in sedimentary archives [37]. This approach was pioneered for regions that underwent periods of low dynamic topography, such as the *Cretaceous Interior Seaway* of North America (e.g. [38,39]), where the associated surface depressions created accommodation space to preserve sediments.

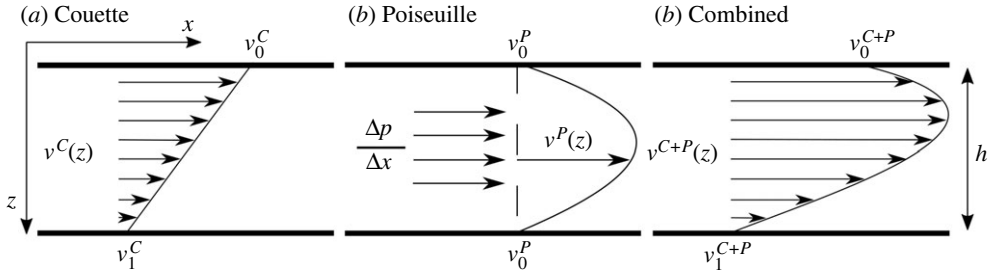

Figure 1. Schematic of (*a*) Couette flow, described a linear profile of shear driven fluid motion between two surfaces where one moves tangentially relative to the other, and seen as proxy for passive asthenosphere flow driven by motion of the overlying plate, (*b*) Poiseuille flow, described by a parabolic profile, driven by a lateral pressure gradient, and seen as a proxy for active asthenosphere flow capable of driving the overlying plate, and (*c*) superposition of both.

It is more difficult to map the stratigraphic expression of dynamic topography highs. The associated elevated topography creates erosional/non-depositional environments expressed as time gaps in the geologic record. The resulting discontinuity surfaces in sedimentary archives are known as non conformities and unconformities (see [40] for a review). They preserve time missing (hiatus) from the geological record [41]. To this end, an approach of hiatus-area mapping was introduced by Friedrich *et al.* [41] and Friedrich [42]. It visualizes interregional-scale unconformities because, at continental scales, what is normally perceived as a lack of data (material eroded or not deposited) becomes part of the dynamic topography signal. The method has been applied to map the spatio-temporal patterns of conformable and unconformable geological contacts across Europe [43], Africa [44] and the Atlantic realm and Australia since the Upper Jurassic [45,46]. An important finding is that significant differences exist in the spatial extent of hiatus area across and between continents at the timescale of geologic series, that is ten to a few tens of Myrs (see definition of series as a unit of chronostratigraphy in the chronostratigraphic chart [47,48]). This is considerably smaller than the mantle transit time, which as the convective timescale is about 100–200 Myrs [33] for Earth's mantle. The difference between the convective timescale and the timescale for topography in convective support suggests vigorous upper mantle flow, as illustrated by geodynamic kernels (see [49] for a review).

Pressure driven asthenosphere flow explicitly relates plate motion changes, induced by evolving basal shear forces, to non-isostatic vertical motion of the lithosphere, as noted before. Such correlations were reported for the South [32] and North [43] Atlantic. Here, we extend this observational geodynamic approach. We take the hiatus maps of Hayek *et al.* [45,46], with an updated dataset for Australia following the approach of Carena *et al.* [44], as proxy for mantle flow induced vertical lithosphere motion and compare them systematically to horizontal plate motion variations deduced from a past plate motion model based on the dataset of Müller *et al.* [27]. We organize our paper as follows: §2 and 3 provide brief summaries of plate motion variations and hiatus surfaces for the Atlantic and Indo-Australian realm. We study these regions to account for ocean basins with and without significant subduction activity, while our choice of the Upper Jurassic as the starting point of our analysis is motivated by geodynamic considerations on the mantle transit time, to remain within a timescale comparable to a mantle overturn [33]. We then analyse spreading rate variations and hiatus surfaces, finding they frequently correlate, except when plate boundary forces may play a significant role. Section 5 places our results into the context of geological studies. This is followed by a discussion on geodynamic implications, where we employ Poiseuille/Couette models for scale analysis. Finally, we draw conclusions in §6.

2. Oceanic spreading rates

Figure 2 presents the spreading rates of the seafloor at the time of crustal creation as a data grid from Seton *et al.* [50] based on the GTS2012 [51] timescale (see [54] for a discussion of

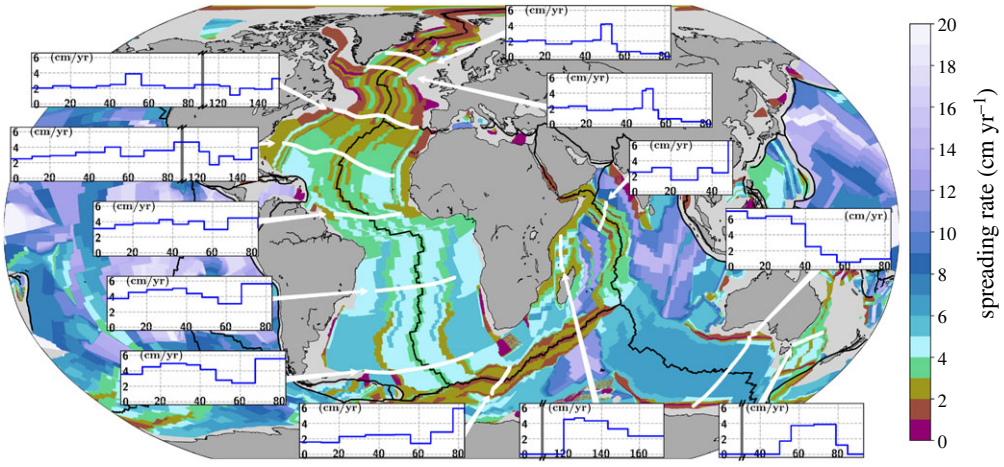

Figure 2. Grid of ocean floor spreading rates reproduced from Seton *et al.* [50] based on GTS2012 [51] timescale. Colours indicate spreading rates at time of crustal creation, revealing frequent spreading rate changes throughout the oceans. Inset figures, where *y*-axis is spreading rate in cm yr^{-1} and *x*-axis time in Ma, show rates at selected locations. Grey vertical lines in the inset plots for the Central Atlantic correspond to the Cretaceous Normal Superchron (CNS), when spreading rates are known only at mean rates across the CNS (see text). For the Indian ocean, they represent omitted time. Profiles extracted from [52] database using *pyGPlates* [53]. (Online version in colour.)

the influence of the timescale choices for the uncertainty of reconstructed spreading histories). We also superpose profiles of relative spreading rates throughout the Atlantic, the Indian and the Southern Ocean south of Australia, extracted with *pyGPlates* [53] from the latest dataset of Müller *et al.* [52], to bring out local spreading rate variations. Most of the inset spreading rate profiles are reported for the time from 80 Ma onward, whereas profiles in the oldest ocean floor regions, such as the Central Atlantic and Madagascar, are shown from earlier times onward. The Cretaceous Normal Superchron (CNS) restricts the temporal resolution of Cretaceous spreading rates to mean values [27,55], therefore we omit the report of spreading rates spanning this time period.

Overall, figure 2 reveals that rapid spreading rate variations (less than 10 Myrs) occurred throughout the oceans, with spreading rates in the South Atlantic and the Antarctica-Australia spreading centre (~ 6 cm yr^{-1}) being faster compared to rates in the North Atlantic (~ 2 cm yr^{-1}). The inset profiles from north to south for the Atlantic show distinct temporal variations. The North Atlantic rates have a noticeable peak of ~ 4 cm yr^{-1} in the early Eocene from ~55–45 Ma that follows the onset of spreading in the region. They drop to ~ 2 cm yr^{-1} in the last 45 Ma. The South Atlantic is characterized by higher rates and larger variations. At 80 Ma, near the end of the CNS, nominal rates are ~ 6 cm yr^{-1}. In the Paleocene, from ~65 to 55 Ma, they drop by a factor of three to ~ 2 cm yr^{-1}, followed by a renewed increase up to a peak of ~ 6 cm yr^{-1} at ~30 Ma. From ~25 Ma onward, rates decrease to ~ 4 cm yr^{-1}. The Central Atlantic is a superposition of trends from the south, i.e. slow rates in the Paleocene (~ 3 cm yr^{-1}) around 60 Ma, and from the north, i.e. a peak in the early Eocene at ~50 Ma (~ 4 cm yr^{-1}). The spreading rate profile between India and Africa in the Indian ocean shows two peaks of ~ 3 cm yr^{-1} each. One lasts from ~40 to 35 Ma, the other from ~20 to 10 Ma, separated by a minimum of ~ 1.5 cm yr^{-1} from ~35 to 20 Ma. Prior to 45 Ma, spreading velocities are significantly higher (~ 14 cm yr^{-1}). The Lord Howe Rise profile (east of Australia) shows high spreading rates (~ 4 cm yr^{-1}) from ~80–60 Ma decreasing to zero by ~50 Ma. Conversely, spreading rates in the Southern Ocean south of Australia are near zero (~ 0.5 cm yr^{-1}) from 80 to 60 Ma, increasing from the Paleocene onwards to spreading rates of ~ 6 cm yr^{-1}.

3. Continental Base Hiatus Surfaces

Figure 3 shows Base Hiatus Surfaces (BHS) taken from Hayek *et al.* [45,46] for North and South America, Europe, Africa and Australia for eight geologic series beginning with the Lower Cretaceous. The resolution of geological series is chosen, because this is the most frequently adopted temporal resolution for interregional geologic maps [42]. The choice of the Lower Cretaceous as the oldest stratigraphic unit represents the mantle transit time [33], as noted before. We use the terms *un/conformable* and *hiatus/no hiatus* indistinguishably and follow Friedrich [42], Carena *et al.* [44] and Hayek *et al.* [45]. They define *hiatus/unconformable* as the state when one or more geological series in the chronostratigraphic chart [47,48] immediately preceding the target geological series are missing, regardless of whether either geological series has missing stages. *No hiatus/conformable* is defined as the complementary state. Hiatus is delimited for a given target geological series by any occurrence of the immediately preceding geological series. From hiatus mapped this way, Hayek *et al.* [45,46] construct BHS through a spherical harmonic representation (up to degree 15 and convolved with a Gaussian filter), reconstructed to their past tectonic setting with a global Mesozoic–Cenozoic plate motion model [27] tied to a global moving hotspot reference frame [56] from present-day to 100 Ma and a True Polar Wander (TPW) corrected paleomagnetic reconstruction [58] for times older than 100 Ma. The latter includes a longitudinal shift of 10° incorporated by Seton *et al.* [55]. The surfaces are presented in the plate configuration that corresponds to the base of each geological series.

BHS serves as a proxy for paleotopography and vertical motion of the continents, as suggested by Friedrich *et al.* [41] and earlier authors (e.g. [59]). Red/blue colours depict un/conformable (hiatus/no hiatus) contacts, respectively, indicative of high/low topography in the preceding geological series. Blank regions reveal the absence of the target geological series and its immediately preceding unit. Such regions may have undergone intense and/or long-lasting erosion or non-deposition, indicative of intense and/or persistent exhumation and surface uplift [41–46]. Black dots in each BHS figure mark the current location of the Yellowstone, Canaries, Afar, Iceland and Tristan hotspots [57]. A detailed presentation of the data sources, the BHS construction and the related uncertainties are given in Hayek *et al.* [45].

Overall figure 3 reveals significant differences in hiatus distribution across and between continents at the timescale of geologic series. Described in detail in Hayek *et al.* [45,46], we summarize the main BHS features and recall that BHS at each geological series serves as a proxy for topography in the preceding geological series. *Base of Lower Cretaceous*, figure 3*a*, shows hiatus surface (red) and blank regions, indicative of high topography in the Upper Jurassic, in much of North and South America, Africa and Australia. No hiatus (blue), indicative of low Upper Jurassic topography, is prominent in northernmost Africa and Europe. *Base of Upper Cretaceous*, figure 3*b*, shows hiatus and blank regions in parts of Europe, North and South America. No hiatus is prominent throughout much of Africa, Australia and South America in the Paraná region. *Base of Paleocene*, figure 3*c*, reveals isolated patches of hiatus surface and blank regions along the east coast of Brazil, in Southern Africa (Karoo Basin) and Australia. No hiatus regions dominate elsewhere throughout the continents. *Base of Eocene*, figure 3*d*, presents hiatus surface and blank regions prominently in two continents: Europe, and South America except the Amazon Basin. No hiatus exists in the northernmost part of Africa, the Karoo Basin and eastern Australia. *Base of Oligocene*, figure 3*e*, displays blank regions in Africa. But the foremost occurrence is in South America, where it signals an almost complete absence of Oligocene and Eocene strata throughout the continent. Limited hiatus surface exists in the western part of North America and the Afar region. Europe, northernmost Africa, the Karoo Basin and much of Australia show prominent no hiatus regions. In *Base of Miocene*, figure 3*f*, hiatus surfaces dominate across the continents. Prominent examples include North and South America, parts of Europe, Australia and Africa. North America shows conformable contacts surrounding the hiatus regions near the Yellowstone hotspot location. Alaska, Patagonia and Central Europe also show conformable contacts. *Base of Pliocene*, figure 3*g*, reveals minor hiatus surface and blank regions. Hiatus is located in central Africa and near the Canaries. Blank regions occur in eastern North and South America. No hiatus

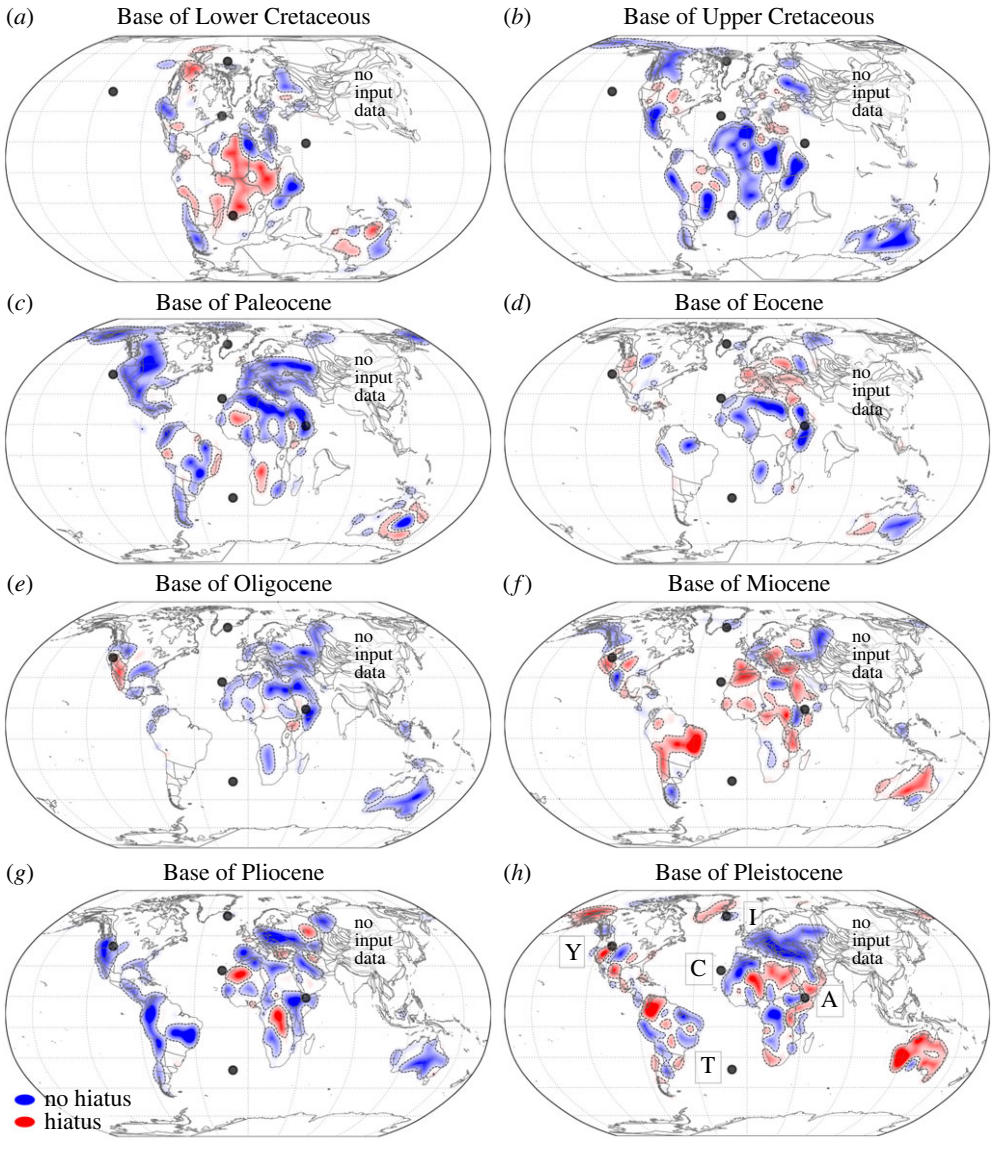

Figure 3. Base Hiatus Surfaces (BHS) from Hayek *et al.* [45,46] for eight geological series from Base of Lower Cretaceous to Base of Pleistocene (*a–h*) reconstructed paleogeographically with a global Mesozoic–Cenozoic plate motion model [27] tied to a reference frame of global moving hotspot and a True Polar Wander (TPW) corrected paleomagnetic reconstruction [56], with the latter updated by Seton *et al.* [55] (see text), and placed into a plate tectonic configuration corresponding to the base of each geological series. Red/blue colours represent the hiatus/no hiatus surfaces. Black dotted lines contour the spherical harmonics signal at the ± 0.1 amplitude. Each map serves as a proxy for paleotopography (red = high, blue = low) in the preceding series (see text). Black dots are current locations of Yellowstone (*Y*), Canaries (*C*), Afar (*A*), Iceland (*I*), Tristan (*T*) hotspot [57]. (Online version in colour.)

signals dominate elsewhere. *Base of Pleistocene*, figure 3*h*, shows North and South America and Africa with a mix of hiatus and no hiatus surfaces. Extensive hiatus surface exists in Australia, except the *Nullarbor Plain*, Alaska, the eastern margin of Greenland and north-central Africa. No hiatus surface prevails in Europe and the Congo Basin. Figure 4 shows BHS with a view centred on North America, to illuminate a continent moving towards a hotspot. Much of the eastern half of the continent reveals blank regions, reflecting the absence of Lower Cretaceous to Pleistocene

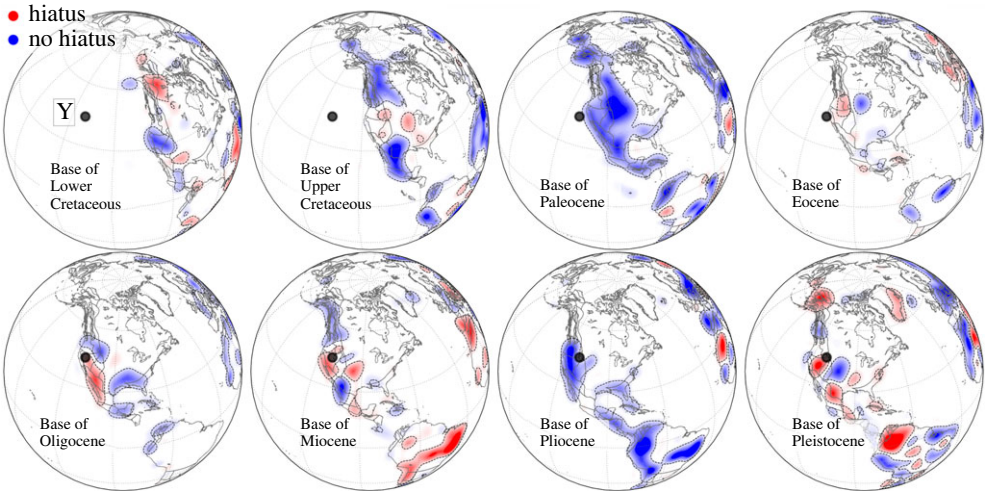

Figure 4. Same as figure 3, but centred on North America. Each BHS map serves as a proxy for paleotopography (red = high, blue = low) in the preceding geological series (see text). Black dot is current Yellowstone (*Y*) hotspot location [57]. From the Base of Eocene to Base of Miocene hiatus signal surrounds the current location of Yellowstone. (Online version in colour.)

series. But, in the western half of the continent, the hiatus surface changes at interregional scales while North America approaches the current location of the Yellowstone hotspot. A prominent change occurs from the *Base of Paleocene* to *Base of Eocene*, when an extensive no hiatus signal transforms to mostly blank regions and hiatus, indicative of growing topography. From the *Base of Eocene* to *Base of Miocene* hiatus signal surrounds the current location of Yellowstone, starting with hiatus to the northeast of the current plume location and leading to hiatus located in the Columbia Plateau regions and the Interior Plains, as noted also by Friedrich *et al.* [41] and Stotz *et al.* [60].

4. Oceanic spreading rates and continental Base Hiatus Surfaces

(i) Atlantic Realm

Figure 5 (top row) shows BHS with a view focused on the North Atlantic/Europe. There are two periods of widespread hiatus in Europe, in the Paleocene and the Oligocene, revealed by hiatus surface at the *Base of Eocene* and *Base of Miocene*, respectively. This is illustrated by a curve (middle row) for proxy elevation, which we construct as the sum (for a given geological series) of hiatus and blank regions, normalized by the total area (Europe) under consideration. The bottom row plots oceanic spreading rates at three transects, north to south, between Greenland and Europe from the beginning of the Upper Cretaceous onward. The spreading rate magnitude increases, as expected, with decreasing latitude and further distance of the transects from the Euler Pole. Importantly, the transects reveal two periods of higher spreading rates: a 10 Myrs peak in the early Eocene and a second increase in the early Miocene. The latter is more pronounced in the two southern profiles. These observations were noted by Vibe *et al.* [43]. Figure 6*a* (top row) displays BHS with a view focused on the South Atlantic. Two periods of widespread hiatus exist for much of Africa and South America, in the Upper Jurassic and the Oligocene, revealed by hiatus surface at the *Base of Lower Cretaceous* and *Base of Miocene*. There are also two periods of prominent blank region (absence of the considered geological series and its immediately preceding unit) for both continents at the *Base of Eocene* and *Base of Oligocene*. That means the maps show neither Paleocene, nor Eocene and Oligocene strata in much of Africa and South America. In the southern half of Africa blank regions also dominate the *Base of Paleocene*. The proxy elevation curves for Africa

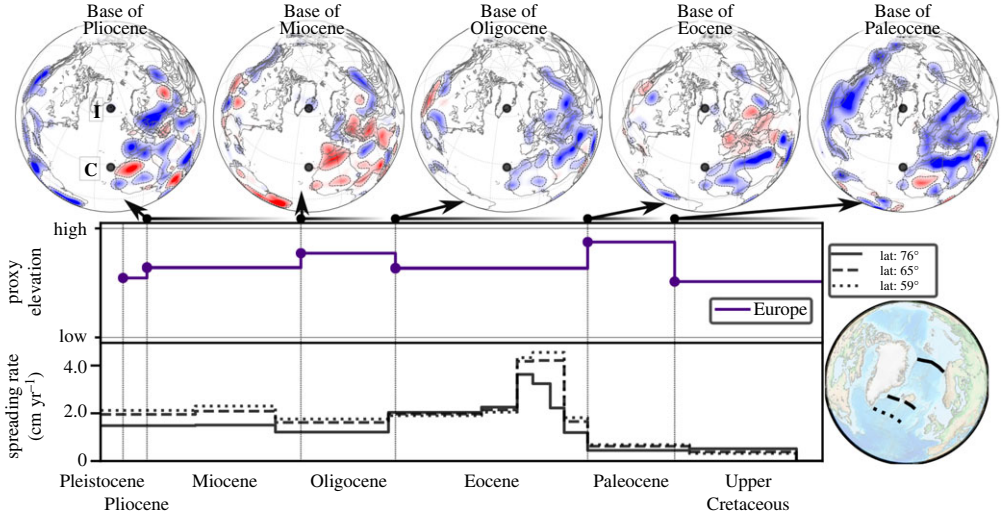

Figure 5. Top row shows BHS centred on the North Atlantic from Base of Pleistocene to Base of Paleocene (see figure 3 caption), with black dots showing the current hotspot locations of Iceland (*I*) and Canaries (*C*) [57]. Middle row shows proxy elevation obtained by the sum of hiatus surfaces and blank regions (see text) for a given geological series normalized by the total area under consideration (Europe). Bottom row shows spreading rates for three transects as indicated in bottom right globe. *X*-axis shows the time range from Pleistocene to Mid Upper Cretaceous. The BHS show prominent hiatus surfaces at the Base of Eocene and Base of Miocene, reflected also as high proxy elevation for the Paleocene and Oligocene. The two proxy elevation peaks are followed by two periods of elevated spreading velocity in the early Eocene and early Miocene. (Online version in colour.)

and eastern South America, figure 6*a* (top part of the two middle rows) normalized to the area of Africa and eastern South America, respectively, bring this out. They show elevated Jurassic topography for both continents, followed by lower topography in the Cretaceous. The African curve increases in the Upper Cretaceous, due to growing proxy elevation in the southern part of the continent, followed by a pronounced continent-scale Oligocene increase. The South American curve instead increases markedly in the Paleocene, and reaches an Eocene peak value. Africa is a large continent, and likely responds to different dynamic topography domains due to its size (see Hayek *et al.* [45,46] and Carena *et al.* [44] for a discussion). To this end, we bring out the different topographic evolution of northern and southern Africa by two proxy elevation curves (lower part of the two middle rows) that are constructed for the northern (plate IDs 714, 715, 503 from the Matthews *et al.* [61] dataset) and southern portions (plate IDs 701, 709, 712, 713 [61]) of the continent, respectively. The curves show a noticeable increase of Upper Cretaceous proxy elevation for southern Africa. Figure 6*a* (bottom row) reports three spreading rate transects for the South Atlantic. Spreading rates are elevated for much of the Cretaceous and the Eocene to mid-Miocene, separated by lower spreading rates in the Paleocene. These observations were noted by Colli *et al.* [32]. Figure 6*b* (top row) depicts BHS with a view centred on the Central Atlantic and northwest Africa. The maps show two hiatus periods, in the Jurassic and the Oligocene, indicated by hiatus surface at the *Base of Lower Cretaceous* and *Base of Miocene*. Two proxy elevation curves, constructed for all of Africa or only for its northwestern sub-region (plate ID 714 [61]), are plotted in figure 6*b* (middle row). Both curves are similar. But the lower value for proxy elevation in the Lower Cretaceous and the peak in proxy elevation for the Oligocene is more pronounced in the northwestern sub-region. Figure 6*b* (bottom row) displays spreading rates for three Central Atlantic transects. They differ from each other in that the northernmost/southernmost transect resembles the spreading rate history of the North/South Atlantic, respectively. For instance, a spreading rate increase in the Lower Cretaceous relates to the South Atlantic transect, while a peak in the early Eocene resembles the spreading rates of the North Atlantic.

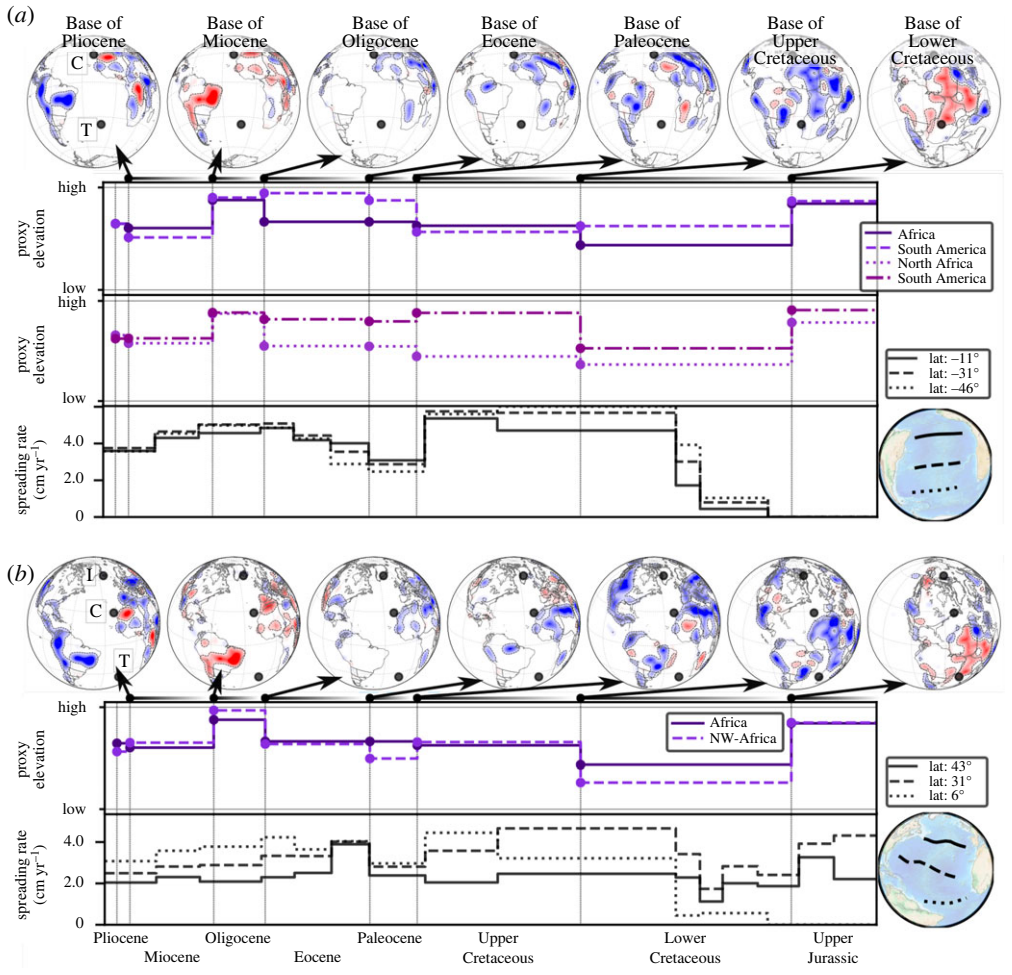

Figure 6. (*a*) Same as figure 5 with top row showing BHS with a view centred on the South Atlantic from Base of Pleistocene to Base of Upper Cretaceous. Black dots represent current hotspot locations of Canaries (*C*) and Tristan (*T*) [57]. Middle rows show proxy elevation curves (see text) for Africa and South America (top) and northern and southern Africa (bottom) from Pleistocene to Lower Cretaceous (see text). Bottom row shows spreading rates for three transects as indicated in bottom right globe. Elevated Jurassic proxy elevation for Africa and South America precedes the spreading onset in the Lower Cretaceous. An increase in Upper Cretaceous African proxy elevation owing to growing elevation in the southern part of the continent (see southern Africa proxy elevation curve) goes along with high Cretaceous spreading rates (see text). A Paleocene increase in South American proxy elevation precedes elevated Eocene spreading rates (see text). (*b*) Same as (*a*) for the Central Atlantic. Black dots in the BHS represent current hotspot locations of Iceland (*I*), Canaries (*C*) and Tristan (*T*) [57]. Middle row shows proxy elevation curves for Africa and its northwestern portion (see text), while bottom row shows three spreading rate transects as indicated by bottom right globe. The northern/southern spreading rate profiles resemble the history of the North/South Altantic respectively (see text). (Online version in colour.)

(ii) Indo-Australian realm

Figure 7 (top row) shows BHS with a view focused on Australia. Extensive conformable area exists at the *Base of Upper Cretaceous*, indicative of low topography in the Lower Cretaceous. Hiatus and blank regions, apart from the Eromanga basin, dominate the *Base of Paleocene*, indicative of overall higher Upper Cretaceous topography. A distinct difference between western and eastern Australia emerges at the *Base of Eocene*, when hiatus/no hiatus surface dominates the western/eastern portion of the continent, respectively. The difference continues at the *Base of*

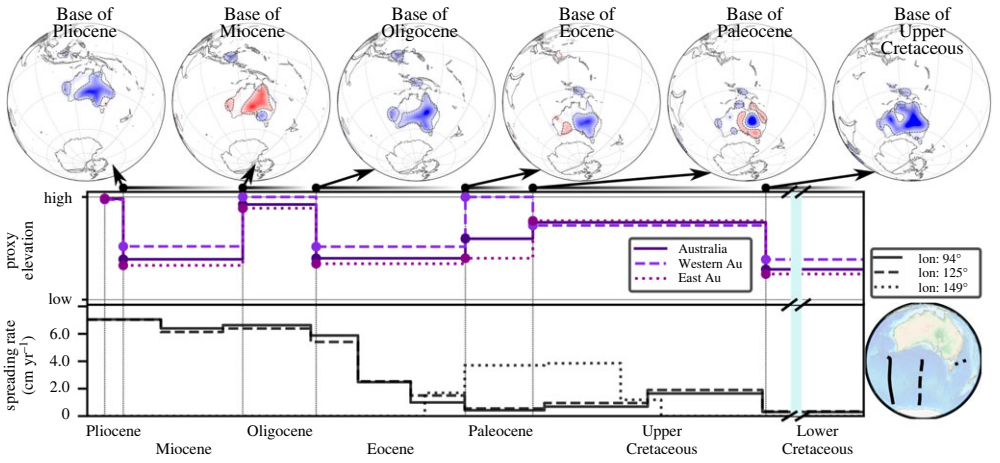

Figure 7. Same as figure 5 with view centred on Australia. Top row shows BHS (see text). Middle row shows proxy elevation curve for the entire continent or separated for eastern and western Australia (see text). Bottom row shows spreading rates for three transects as indicated in bottom right globe. Blue vertical line in the Lower Cretaceous represents a time-lapse omission. Elevated Upper Cretaceous proxy elevation goes along with spreading of Lord Howe Rise (dotted curve), whereas elevated western Australia proxy elevation in the Paleocene precedes rapid Eocene spreading between Antarctica and Australia (see text). (Online version in colour.)

Oligocene, with a blank surface in much of northwestern Australia and no hiatus elsewhere. There is a near continent-wide hiatus surface at the *Base of Miocene*, followed by extensive no hiatus at the *Base of Pliocene*. Proxy elevation curves, figure 7 (middle row), for the entire continent or separated for eastern and western Australia (the separation corresponds to the Western Australia state border, west of 129° present-day longitude) bring these observations out. The continent as a whole experiences an overall proxy elevation increase from the Lower to the Upper Cretaceous and an Oligocene peak value. But there is a marked difference for the eastern and western Australia proxy elevation curves in the Paleocene. The former decreases, the latter increases relative to the Upper Cretaceous. We plot spreading rate transects for the Antarctic-Australia ridge and the Lord Howe Rise in the bottom row of figure 7. The Lord Howe Rise was active to the southeast of Australia from the middle of the Upper Cretaceous onwards, with velocities of $\sim 4\,\mathrm{cm\,yr^{-1}}$. It ceased spreading in the early Eocene, when motion initiated along the Antarctica-Australia ridge. From then on Antarctica-Australia spreading rates increased significantly, reaching $\sim 6\,\mathrm{cm\,yr^{-1}}$ by the Oligocene. The top row of figure 8 displays BHS with a view centred on East Africa, from the *Base of Oligocene* onward. This links to the rise of the Afar plume, for which domal uplift, indicated as well in our maps, has been documented after the early Eocene [62]. Even though the main hiatus surface occurs at the *Base of Miocene*, there is another hiatus at the *Base of Pleistocene*. Proxy elevation curves, figure 8 (middle row), for all of Africa or its northeast sub-region (plate IDs 709, 710, 712, 713, 715, 503 from the Matthews *et al.* [61] dataset) bring this out. The Pliocene increase is more pronounced in the regional proxy elevation curve of East Africa compared to the curve for all of Africa. Figure 8 (bottom row) plots two spreading rate transects for the Carlsberg Ridge since the Upper Cretaceous. They show minor spreading rate variations from the mid-Eocene onwards.

5. Discussion

It is a geodynamic tenet that plates organize the flow and that they are an integral part of the convective system (see [63] for a review). Yet the precise nature of how plate motions are caused by mantle convection remains incomplete, because the strength of plates conceals the underlying

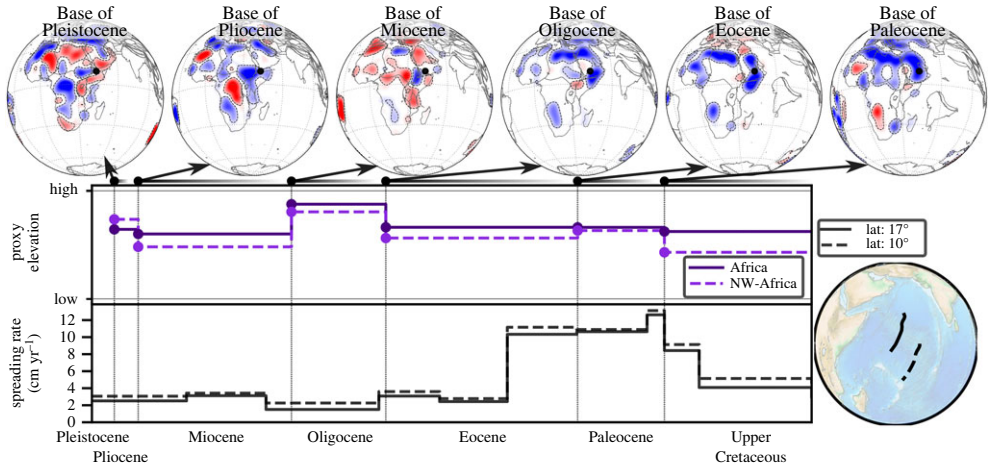

Figure 8. Same as figure 5 with view centred on Eastern Africa. Top row shows BHS (see text) with black dot representing the current hotspot location of Afar (*A*) [57]. Middle row shows proxy elevation curve for the entire continent or its northeast subregion (see text). Bottom row shows spreading rates for two transects as indicated in bottom right globe. Growing East Africa proxy elevation in Paleocene–Oligocene and decreasing Carlsberg spreading rates, presumably reflect plate boundary forces from India-Asia Collision (see text). (Online version in colour.)

flow. The description by Morgan *et al.* [16] and Höink *et al.* [19–22] of asthenosphere flux in terms of Poiseuille/Couette flow offers a way to overcome this difficulty by mapping upper mantle flow through its topographic and viscous effects. This geodynamic perspective motivates us to compare changes of oceanic spreading rates and continental hiatus surface, by building upon earlier work and exploiting growing observational constraints on both.

A link between spreading rate variations and dynamic topography is perhaps best evinced for the North Atlantic (figure 5), where two periods of expanding hiatus surface across Europe in the Paleocene and Oligocene precede the Eocene spreading onset and faster Miocene spreading rates, as noted by Vibe *et al.* [43]. The region is well suited for an observational geodynamic analysis. Its Cenozoic opening history has left well-preserved sea-floor magnetic lineations (e.g. [64,65]) and hiatus surfaces. There are also well-documented regional uplift episodes reported, for instance, for the British Isles, Greenland, Scandinavia and Central Europe (e.g. [66–69]). Reviews of uplift and subsidence events across the region are given by various authors [70–72]. The region also contains prominent plume systems. They provide a geodynamically plausible mechanism to drive active upper mantle flow, as suggested by scaling analysis [21]. Plume systems at the western edge of Europe include the Canaries, which experienced Oligo/Miocene uplift at the local [73] and regional scale [74], and the Iceland-Jan Mayen system. The broad extent of the latter was imaged seismically by Rickers *et al.* and Celli *et al.* [75,76]. Importantly, studies of the Iceland-Jan Mayen system reveal temporal mass flux [77] and thermal anomaly [78] variations, with peaks in the early and late Cenozoic. Our results support these accounts of temporal system variations and indicate their interregional scale, documenting early Paleogene and Neogene changes in dynamic topography and spreading rates, induced presumably through variations in pressure-driven upper mantle flow.

The opening history of the South Atlantic realm, which hosts the Tristan hotspot, spans nearly three times that of the North Atlantic, reaching back into the Mesozoic. But links between spreading rates and dynamic topography are more difficult to establish, because the early South Atlantic opening falls largely within the CNS, restricting the interpretation of Cretaceous spreading rates to mean values, and because the long duration of the Lower/Upper Cretaceous series (approx. 40 Myrs each) limits the temporal resolution of our geological series-based hiatus mapping during that time. The main observation is a bimodal spreading rate distribution, with

Cretaceous and mid-Cenozoic peaks separated by a Paleocene low, as seen in our results and pointed out by Colli *et al.* [32]. This goes along with high Upper Jurassic proxy elevation for Africa and South America, and renewed proxy elevation for southern Africa in the Upper Cretaceous and for South America starting in the Paleocene. But observations beyond this first order division are beginning to emerge. For the phase preceding the South Atlantic opening, Krob *et al.* [79] use geological archives (stratigraphic and thermochronological data) and stratigraphic frameworks to document interregional-scale Upper Jurassic uplift in South America and Africa, which they link to the Paraná-Etendeka plume rise well in advance of flood basalt eruptions and the onset of seafloor spreading. For the CNS, and using a new identification of magnetic anomalies located within that time period, Granot & Dyment [80] report accelerating rather than constant South Atlantic spreading rates, with a peak achieved in the early Campanian (approx. 80 Ma). This goes along with increasing Upper Cretaceous proxy elevation in southern Africa (figure 6*a*) and a growing consensus about the uplift history of the South African Plateau (SAP). Reports on the latter assign Upper Cretaceous ages to peak sediment flux (e.g. [81–83]) around the SAP, increased kimberlite occurrence in southern Africa [84], and basin inversion and margin tilting along the Namibian coast [85,86], consistent with a Late Cretaceous SAP uplift pulse inferred from thermochronological studies [87,88]. No major coeval activity is indicated for the Tristan hotspot. But the ∼85 Ma eruption of the Marion hotspot [89,90] occurs at a geodynamically relevant distance (approx. 2000 km east of southern Africa) addressed in the next section. The Tertiary phase of the South Atlantic opening has accelerated spreading rates starting in the Eocene, preceded by growing South American proxy elevation (figure 6*a*) in the Paleocene. The interregional scale of this event is evinced by a variety of studies. They document a Paleogene hiatus in Andean Foreland Basins [91], regional uplift along the Argentine margin [92], and an Eocene reactivation of the South American passive margin (e.g. [93–95]) deduced from landscape analysis and thermochronological data. Far field effects from plate boundary forces associated with the Andean margin [93] have been invoked to explain these events. But most studies agree that prominent uplift of the Andes started in the mid Eocene, reaching a peak in the Oligocene, with a second uplift period in Late Miocene [96]. It is not obvious how increased topographic loads from the Andes would induce faster South Atlantic spreading. Instead, there are reports for anomalously young (late-stage) volcanism (≈46 Ma) on the Rio Grande Rise (RGR) and an Eocene subaerial exposure of the RGR at Drill Site 516 [97,98]. They point to temporal flux variations of the Tristan hotspot, similar to what is reported for Iceland. This should be considered in future geodynamic analyses of the basin. A review of Cretaceous-Cenozoic sediment supply to the South Atlantic margins and the complex uplift and subsidence history of the region is given by MacGregor [99].

Links between spreading rates and dynamic topography for Australia must acknowledge the onset of subduction in the Cenozoic of the Indo-Australian plate beneath Southeast Asia (e.g. [100]), so that the geodynamic setting of this region differs fundamentally from the Atlantic realm. Australia's dynamic topography history from the Jurassic onward has been reviewed by Harrington *et al.* [101] and involves several key observations. Long-wavelength tilting since the late Cretaceous (e.g. [102,103]) occurred when the continent approached the subduction systems of Southeast Asia on its northward passage. It is manifested by high Miocene subsidence rates on the Australian northwest shelf inferred from the stratigraphic architecture of carbonate platforms [104]. River profile studies provide additional constraints. They report regional uplift for western and central Australia starting in the Eocene (e.g. [105,106]) and a two-stage uplift history for the Eastern Highlands. A first stage, from 120 to 80 Ma, coincided with rifting along the eastern margin, whereas a second stage, inferred broadly for 80–10 Ma, formed the Great Escarpment [106]. A third and long-standing observation relates to Australia's flooding record. Its maximum occurs in the Lower Cretaceous, when the Eromanga and Sutra basins in the eastern half of the continent experienced marine inundation. The discrepancy of Australia's flooding record with global sea-evel curves (e.g. [107]) was noticed early on and prompted pioneering geodynamic studies that attributed the inundation to Australia's passage over a slab associated

with Gondwana subduction (e.g. [108,109]). Our results agree with these findings and document the interregional nature of Australia's topographic changes. They show that spreading onset of the Lord Howe Rise went along with a proxy elevation growth from the Lower to the Upper Cretaceous, although a detailed analysis is limited by the long duration of the Lower/Upper Cretaceous series. The interregional scale of this elevation change suggests the involvement of active mantle flow. Several studies have attributed Lord Howe spreading to a mantle upwelling (e.g. [110–112]). Supporting evidence comes from geochemical data tracing a deep mantle (HIMU) component in Upper Cretaceous volcanics in Zealandia [113]. Active plume-driven flow in the Upper Cretaceous at Australia's eastern edge would indeed provide a plausible link between the topographic and spreading signal at that time. By contrast, no plume activity has been invoked, to our knowledge, for Western Australia's proxy elevation growth in the Paleocene, which preceded the Eocene onset of Antarctic/Australia separation (figure 7). However, Stotz *et al.* [114] used coupled mantle circulation and tectonic models to suggest that Poiseuille flow inherited from Mesozoic mantle circulation led to the Eocene separation of Australia and Antarctica, eventually inducing subduction of the Indo-Australian plate beneath Southeast Asia and high spreading rates along the Antarctica-Australia ridge.

Links between dynamic topography and plate motion variations are perhaps least evinced in our maps for the Indian Ocean realm, because collisional forces associated with India-Eurasia convergence arguably make this ocean basin the one currently most strongly influenced by plate boundary forces. Several studies argue for significant edge forces in the region as a result of topographic loads associated with the region's orogenic plateaus [115,116], amounting to $\sim 5\text{–}10 \times 10^{12}\,\mathrm{N\,m^{-1}}$ [117,118], sufficient to reduce India's plate motion [117]. Additional complexity seemingly arises from temporal flux variations of the Reunion plume [119,120]. Not surprisingly, our results reveal growing East Africa proxy elevation in the Paleocene–Oligocene and simultaneous decreasing Carlsberg spreading rates, which presumably reflect expanding boundary forces from India-Asia collision, and minor spreading rate variations in the late Paleogene and Neogene, at the time of the Afar plume arrival. Figure 9 summarizes our findings and reveals the correlation between high proxy elevation and subsequent spreading rate changes with grey boxes for the studied regions from Upper Jurassic to Pliocene.

Our discussion must acknowledge the influence of eustatic contributions to the proxy elevation curves. For instance, there is an increase in the Oligocene proxy elevation curve for all regions considered, see hatched area in figure 9. In Hayek *et al.* [45,46] we bring out the sea-level signal by plotting the temporal evolution of no-/hiatus surfaces in the BHS separately for individual continents and combined for all continents considered. This reveals two prominent continent-wide maxima in the BHS at the Base of Miocene and Base of Pleistocene corresponding to high proxy elevation curves in the Oligocene and the Pliocene, respectively. The latter coincide with the onset of glaciation in Antarctica and the Northern Hemisphere, respectively. This suggests caution in the interpretation of Oligocene and Pliocene hiatus.

Our discussion of the comparison of hiatus surfaces and past plate motion changes must emphasize the severe limitations of the input data for our hiatus mapping method. Addressed in detail by Hayek *et al.* [45], we recall first that the BHS are well constrained in lateral extent but not in amplitude. The latter requires independent calibration, for example, by using thermochronological data [121]. Second, that the temporal resolution of interregional hiatus analysis depends on the temporal resolution of the input geological maps. At continent scale, they are currently limited to the geological series level. The limitation is aggravated because hiatus is likely longer than indicated by the missing geological series (see fig. 3 in [42]). At any one location sedimentary successions may represent only a small portion of a geological series. This implies large temporal uncertainties in our analysis, inevitably hiding shorter duration lacunae and favouring large time intervals. The severe limitations of the input data can be alleviated with additional geologic indicators, which are beginning to yield powerful constraints on past dynamic topography. They include paleoaltimetry estimates [122], studies of river profiles (e.g. [123]), landforms [124] and sediment provenance [62,125], constraints from thermochronological

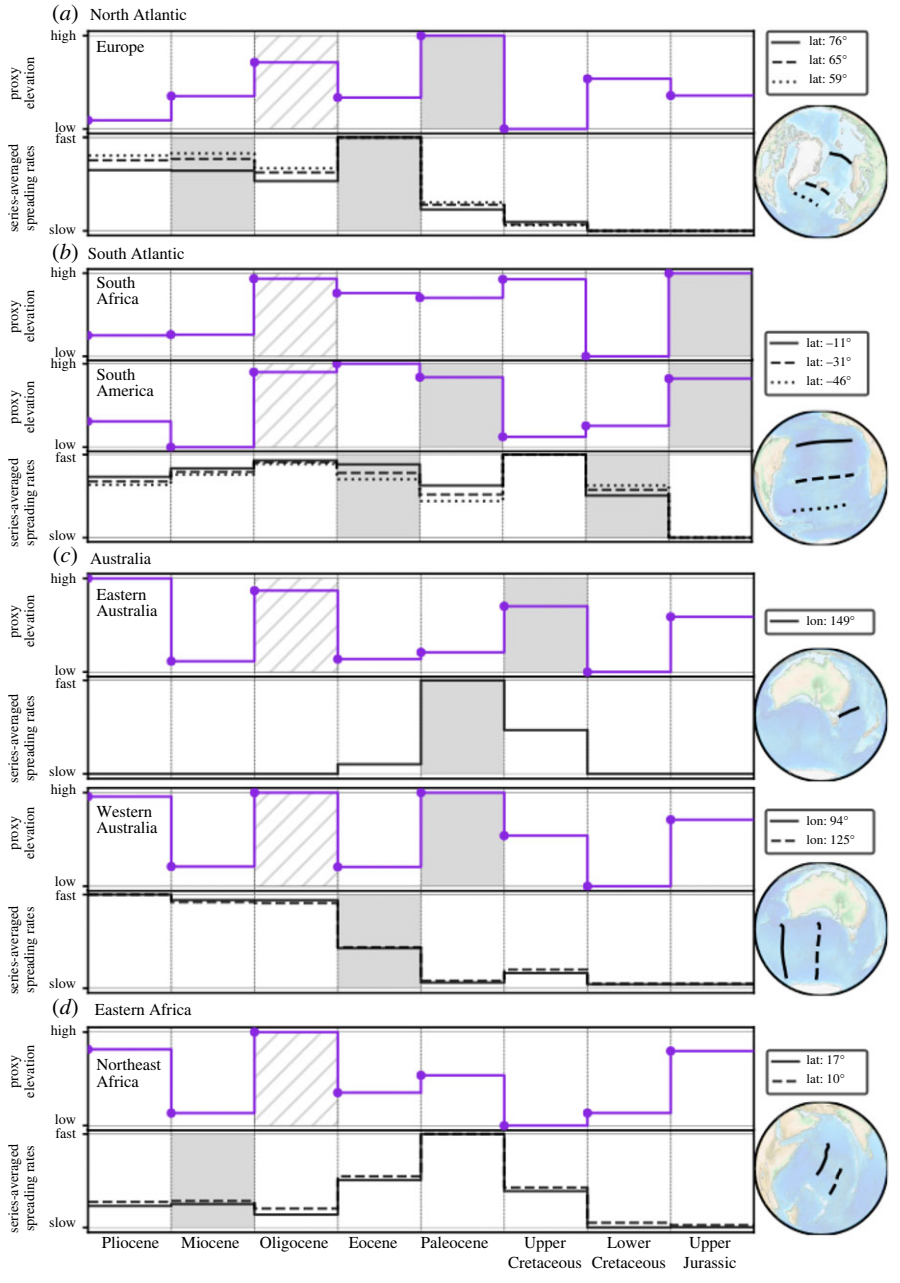

Figure 9. Summary figure showing correlation between high proxy elevation (PE) and subsequent spreading rate changes with grey boxes for studied regions from Upper Jurassic to Pliocene. PE curves (dot marks the datum) are normalized to their minimum/maximum, spreading rates are averaged over each geological series, and all series are represented with the same length. (*a*) North Atlantic: high Paleocene PE followed by Eocene spreading onset. (*b*) South Atlantic: high Upper Jurassic South African/South American PE followed by Lower Cretaceous spreading onset. High Paleocene South American PE followed by Eocene spreading rate increase. (*c*) Australia: high Upper Cretaceous Eastern Australia PE followed by peak Paleocene Lord Howe Rise spreading rates. High Western Australia Paleocene PE followed by Eocene Antarctica-Australia spreading onset. (*d*) Eastern Africa: growing Paleo/Oligocene PE and simultaneous decreasing Carlsberg spreading rates presumably reflect boundary forces from India-Asia collision. High Oligocene PE (hatched box) in part reflects eustatic signal from Antarctic glaciation onset [45,46]. Long duration of Upper/Lower Cretaceous series combined with Cretaceous Normal Superchron mask relation between PE and spreading rate changes (e.g. high Upper Cretaceous South African PE and South Atlantic spreading rates, see text).

[126–128] or paleobiological and paleoenvironmental data [129], as well as quantifications of sediment budgets at the scale of continental margins [81–83,130]. Observational constraints on current and past dynamic topography are reviewed very effectively by Hoggard *et al.* [131]. Efforts to better constrain past continental vertical motion are matched by similar efforts to improve our knowledge of horizontal past plate motion. Progress is underway to map past plate velocities from sea-floor magnetic lineations at temporal resolutions of ∼1 Myrs or less (e.g. [28,29]) when mitigating for finite-rotation noise [30]. In combination, these efforts should help to further constrain the recent geologic history of large-scale horizontal and vertical lithosphere motion, greatly assisting in geodynamic interpretations of plate driving and resisting forces.

Geodynamic implications

Geodynamicists have long understood the effects of an asthenosphere on mantle flow in modulating the amplitude of dynamic topography and the horizontal flow range (e.g. [4,11]). Our analysis extends these results to geologic observations and suggests a timescale, on the order of a geological series, between the occurrence of continent-scale hiatus and plate motion changes. A similar timescale comes from fluid dynamic studies reporting a delay between domal uplift and magmatism above starting plumes (e.g. [132,133]). These studies are reviewed very effectively by Campbell [134]. The timescale is interpreted best through dynamic topography response functions of dynamic Earth models, because a weak upper mantle delays significant surface deflections into the final phase of material upwellings, when buoyant flow enters from the lower into the upper mantle (see [49] for a review). Our analysis also suggests a spatial scale for interregional hiatus, on the order of 2000–3000 km in diameter. The latter again agrees with starting plume studies, where it is attributed to plume heads flattening by lateral upper mantle flow [134].

Our maps offer the opportunity to compare hiatus size with predictions from fluid dynamic models of Poiseuille/Couette flow (figure 1), following Stotz *et al.* [135]. Figure 10 shows analytic upper mantle flow estimates, derived from the assumption of Couette flow, Poiseuille flow and the superposition of both, at the time when the Yellowstone, Canary, Afar, Iceland and Tristan plumes presumably arrived in the asthenosphere, as evinced by the onset of widespread volcanism [57]. Couette flow (first column figure 10), induced in the underlying asthenosphere by tectonic plate motion, is computed from the reconstructions of Müller *et al.* [27] tied to a global moving hotspot reference frame [56] from present-day to 100 Ma and a TPW corrected paleomagnetic reconstruction [58] for times older than 100 Ma, with the latter including a longitudinal shift of 10° incorporated by Seton *et al.* [55]. This flow is half the surface velocity at mid-asthenosphere depth. Poiseuille flow, induced by a plume-generated pressure gradient in the asthenosphere, is obtained from the equation

$$V_{\text{Poiseuille}} \approx \frac{D^2}{8\mu}\frac{\Delta p}{\Delta x}, \tag{5.1}$$

where D is the asthenosphere thickness, and μ is its viscosity. Both values are tied together by inferences from post-glacial rebound (e.g. [136]). We choose a thickness of 110 km and a viscosity of 5×10^{19} Pa s. $\Delta p/\Delta x$ is the flow inducing pressure gradient, which we estimate from values for density contrast, gravity and dynamic topographic height in $\Delta p = \rho g h$, respectively. We use a density contrast of 3300 kg m^{-3} and a height of 1400 m (e.g. [131]). Δx is the distance away from the plume centre. Equation (5.1) is singular at the plume centre $\Delta x = 0$. To this end, we introduced a cut off at 15 cm yr^{-1} which corresponds to a distance of ∼200 km from the plume source. Poiseuille flow (second column figure 10) is radially symmetric, as expected, decays away from the respective plume centres with velocities > 15 cm yr^{-1}, maintains velocities ∼ 5 cm yr^{-1} at a distance of ∼1000 km from the plume, and decays further farther out. We note that our estimated Poiseuille flow velocities agree with inferences from geologic observations and dynamic models [137,138]. The combined flow (third column figure 10) is derived by adding up the Couette and Poiseuille flow as in Stotz *et al.* [135]. It varies geographically due to the Couette component, such

that different locations experience different upper mantle flow for any given Poiseuille source. We highlight, as a proxy for active mantle flow, those areas where Poiseuille flow exceeds Couette flow by at least 0.5 cm yr^{-1}. These areas are larger under slow moving plates, as expected, and have an extent of ~ 0.4–0.9×10^7 km^2, comparable to the hiatus area inferred from our maps. Our results allow us to evaluate, to first order, the ability of Poiseuille flow to initiate spreading rate changes, following Iaffaldano & Bunge [33].

$$A_f = \frac{\Delta v_p}{\Delta v_f} A_p. \tag{5.2}$$

Equation (5.2) relates the Poiseuille flow dominated area (A_f) to the area (A_p) affected by the spreading rate change. The latter is the entire plate. This relation is modulated by the ratio of the mean pressure-induced velocity change (Δv_f) to the plate velocity change, that is the spreading rate variation (Δv_p). It means that small Poiseuille flow dominated areas (A_f) can affect large plates areas (A_p), provided the mean pressure-induced velocity change (Δv_f) exceeds the plate velocity change (Δv_p). We assume a mean value $\Delta v_f \sim 5$ cm yr^{-1} over a radius of ~1500 km away from the plume centre, a Poiseuille flow dominated area $A_f \sim 10^7$ km^2, and an average plate area $A_p \sim 5 \times 10^7$ km^2 for our analysis, noting that the current size of the African plate is $\sim 6.2 \times 10^7$ km^2, whereas the size of the South American plate at the end of the Cretaceous, shortly before it resumed rapid spreading in the Eocene, was $\sim 2.5 \times 10^7$ km^2. Our analysis shows that plume-driven flow may induce spreading rate changes (Δv_p) on the order of ~ 1 cm yr^{-1} for average-sized plates, comparable to the values reported in our study. Finally, we compute the linear force density associated with Poiseuille flow, for which we estimate plate basal shear stresses from the relationship

$$\tau = \mu \frac{\Delta v_f}{d}, \tag{5.3}$$

where τ is the shear stress generated at the plate base, μ is the asthenosphere viscosity, Δv_f is the velocity difference between plate and asthenosphere flow at mid depth and d is half the asthenosphere channel thickness. Taking an asthenosphere viscosity of 5×10^{19} Pa s, a velocity of 5 cm yr^{-1}, and a half-thickness of 55 km, as noted before, we obtain shear stresses of ~1.5 MPa, in agreement with values reported from instantaneous and time-dependent geodynamic models [139–143]. The spatial coherence of Poiseuille flow evinced from our maps allows us to integrate the shear stress along flow lines. We take a distance of ~1500 km, the radius achieved by Poiseuille flow dominated areas (fourth column figure 10) and obtain linear force densities of $\sim 2.25 \times 10^{12}$ N m^{-1}, comparable to ridge push values, which are estimated to $\sim 2 \times 10^{12}$ N m^{-1} ([144] and references therein). Our estimates agree with earlier studies that have called for strong plume push forces [145], related, for instance, to the Reunion hotspot [119,146,147]. However, we point to the limitation of our analysis, having assumed for the sake of simplicity a Newtonian upper mantle. Strong evidence exists for a Non-Newtonian upper mantle rheology [148]. This would induce more complex upper mantle flow, as indicated by recent geodynamic models [149].

We must also acknowledge that our analysis for the sake of simplicity ignores lateral variations in asthenosphere thickness related to lithospheric thickness variations and the presence of cratonic keels. The latter would have important effects on the flow, particularly by reducing the extent of Poiseuille flow dominated area beneath these cratonic roots. Furthermore, we calculate the Poiseuille flow keeping the plume strength constant for the plumes considered. However, there are growing constraints on a time-dependent plume flux in the upper mantle, as indicated by numerous studies that attempt to estimate plume strength histories (e.g. [62,73,137,150]).

We close with some implications, starting with the Poiseuille flow dominated area A_f computed for the Tristan hotspot (fifth row, fourth column figure 10) at 133 Ma. The area is approximately three times smaller than A_f computed for the more recent Cenozoic plume events (fourth column figure 10). Moreover, the small size contrasts with the large hiatus mapped at the *Base of Lower Cretaceous*, figure 3*a*, for Africa and South America. This result is a consequence of the large Couette flow inferred at that time for the upper mantle beneath Africa and South America

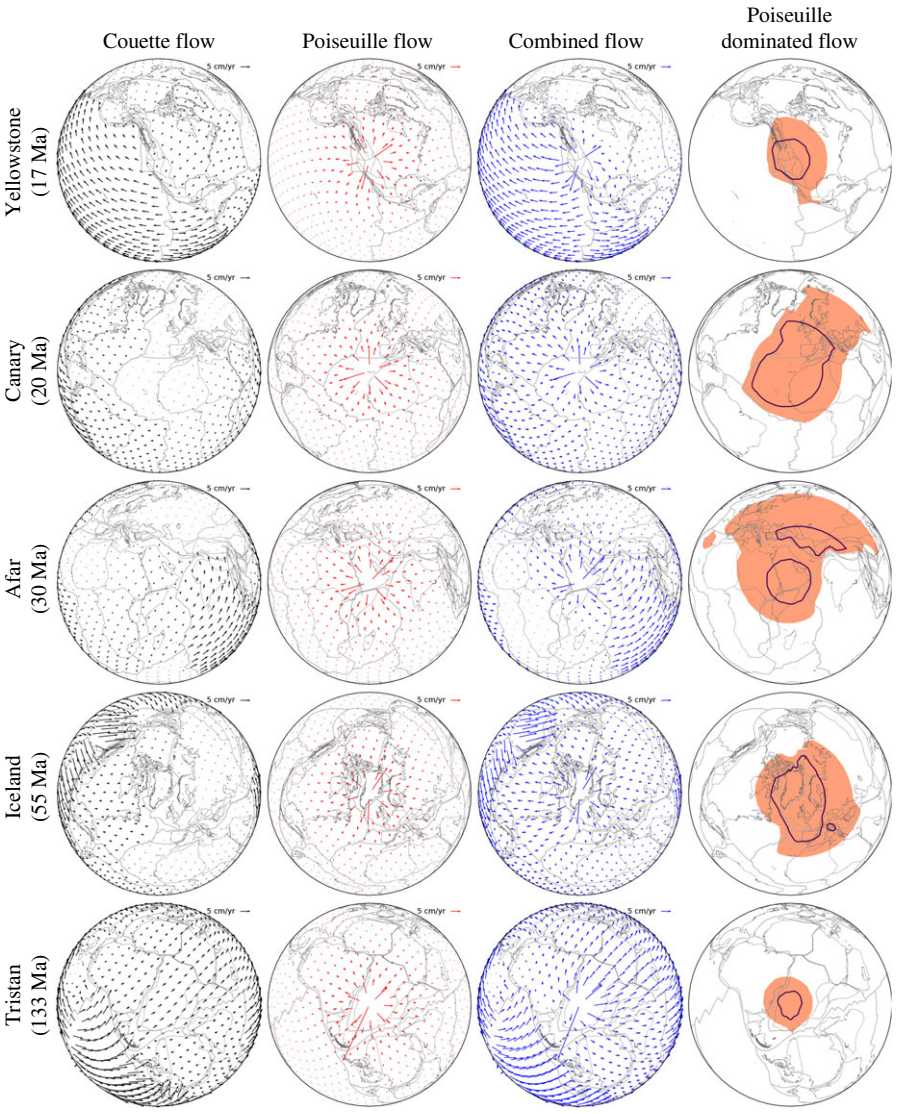

Figure 10. Upper mantle flow estimates based on Couette (black, first column) and Poiseuille (red, second column) models (compare figure 1), and the superposition of both (blue, third column), for a global Mesozoic–Cenozoic plate motion model [27] tied to a reference frame of global moving hotspot and TPW corrected paleomagnetic reconstruction [56], with the latter corrected by Seton *et al.* [55] (see text), shown at mid-asthenospheric level for the time when the Yellowstone, Canary, Afar, Iceland and Tristan plumes presumably arrived in the asthenosphere (see text for details). Poiseuille-dominated flow regions, as indicated by areas where Poiseuille flow exceeds Couette flow by at least 0.5 cm yr^{-1}, are shown in colour in column four. These regions are larger under slow-moving plates and comparable to the hiatus area inferred from our maps (compare figure 3, see text for details). Note the small size for the Poiseuille flow dominated region of Tristan compared to the other hotspots. Blue continuous line contours Poiseuille dominated area when the Poiseuille flow strength is reduced to half the reference value (see text). (Online version in colour.)

from the assumed plate motion model [27]. The latter is tied to a global moving hotspot reference frame [56] from present-day to 100 Ma and a TPW corrected paleomagnetic reconstruction [58] for times older than 100 Ma, which also includes a longitudinal shift of 10° incorporated by Seton *et al.* [55]. O'Neil *et al.* [151] drew attention to the effects of absolute reference frames in past plate motion models, which may include TPW corrections and may assume fixed or moving

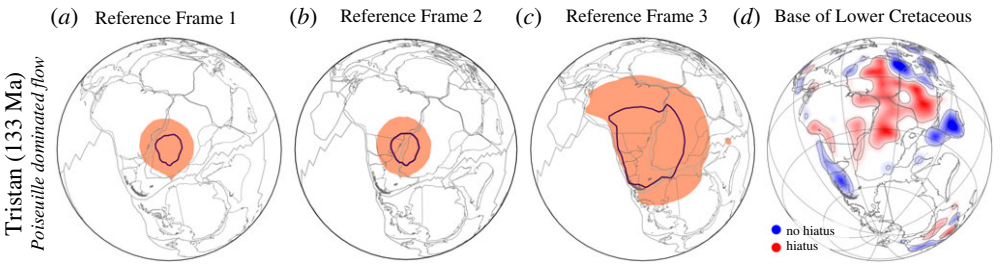

Figure 11. Estimates of Poiseuille flow dominated areas computed for Tristan at 133 Ma using three absolute plate motion models. Panel (*a*) is the same as figure 10 and assumes a global Mesozoic–Cenozoic plate motion model [27]. Panel (*b*) uses an Indo-Atlantic moving hotspot reference frame [151] for the past 100 Myrs and a TPW corrected paleomagnetic model [58] for older times. Panel (*c*) applies a reference frame of Indo-Atlantic moving hotspots [151] for the last 100 Myrs and of fixed African hotspots [155] for prior times. (*d*) BHS for Base of Lower Cretaceous (figure 3). Note that the size of hiatus and blank areas throughout Africa and South America in the Base of Lower Cretaceous map compares well to the extent of the Poiseuille-dominated area in Reference Frame 3. (Online version in colour.)

hotspots or combinations of both. For times < 80 Ma, the reference frame differences are not discernible. But they grow further back in time. Moving hotspot reference frames have been computed from geodynamic models through so-called backward advection (e.g. [152]), which introduces uncertainties related to model parameters and starting conditions. It is possible that backward advection may mispredict Cretaceous hotspot motion, with consequences for plate motion reconstructions, and it is also possible that TPW corrections may overcompensate for the reorientation of the lithosphere-mantle system. Studies exist on absolute reference frame choices in geodynamic models (e.g. [153,154]). But further investigations and the use of mantle flow retrodictions (e.g. [142,143]) seem advised for improved assessments of past hotspot motion. The influence of absolute reference frame choices on the extent of Poiseuille-dominated area is explored in figure 11.

Next, we recall that Hayek *et al.* [45,46] interpreted hiatus maps in terms of the plate and plume mode of mantle convection (see [63] for a review of these convective modes). Broad conformable surfaces reveal the plate mode, while broad unconformable surfaces and areas of lack of signal express the plume mode. From the repeated appearance of continent-scale hiatus they deduced a significant role for the plume mode, which fits with geodynamic studies placing the total plume heat transport into the range of 10 TW (e.g.[156,157]), that is ∼20–30% of the global mantle heat budget (e.g. [158]). Our results suggest that plate motion variations should be included in this interpretation. Taking the current global RMS plate velocity of 5 cm yr^{-1} [25] as representative and recalling that rapid plate motion variations in the range of $\sim$ 1–2 cm yr^{-1} are potentially linked to the plume mode from our analysis, we speculate that ∼20–30% of overall plate velocities could be attributed to the plume mode.

Finally, we turn to plate boundary forces. Several studies emphasized their role in the Indian Ocean realm [115–118] owing to the topographic load of Tibet, as noted before. Others linked plate motion changes to Tibet's evolving topography (e.g. [159,160]). This interpretation remains under debate [120]. But the significant contribution of topography, which is partially controlled by external processes such climate and erosion, to plate boundary forces may go some way in helping to explain why it remains difficult even with advanced mantle convection models, capable of generating plate-like surface motions, to reproduce the recent history of plate motions [161], as this would have to be parameterized in geodynamic simulations. Global coupled models of mantle and lithosphere dynamics may offer a possibility to address these challenges [114].

6. Conclusion

We have used continent-scale hiatus maps as a proxy for mantle flow induced dynamic topography and compared them with plate motion variations in the Atlantic and Indo-Australian realms since the Jurassic, building upon earlier work and exploiting growing observational constraints on both. We find that oceanic spreading rate changes and hiatus surfaces frequently correlate, except when plate boundary forces may play a significant role. Our work is geodynamically motivated from the description of asthenosphere flow beneath tectonic plates in terms of Poiseuille/Couette flow. This description explicitly relates plate motion changes, induced by evolving basal shear forces (Poiseuille flow), to non-isostatic vertical motion of the lithosphere. Our analysis reveals a timescale on the order of a geologic series between the occurrence of continent-scale hiatus and plate motion changes. It is best interpreted through dynamic topography response functions of dynamic Earth models, because a weak asthenosphere delays significant surface deflections into the final phase of material upwellings, when buoyant flow enters from the lower into the upper mantle. Our analysis suggests that the spatial scale of interregional hiatus, which is on the order of 2000–3000 km in diameter, should be interpreted through Poiseuille flow, where it corresponds to regions of active plume-driven upper mantle flow. We use fluid dynamic arguments to show that such active upper mantle flow can induce plate motion changes of ~ 1–$2\,\mathrm{cm\,yr^{-1}}$, comparable to observations. Our results offer the motivation to further improve the temporal resolution of interregional geological maps, to enhance the constraints on past dynamic topography and associated paleogeography. This means such maps should be compiled more directly in relation to the relevant geodynamic processes that are revealed in the geological record. They also motivate one to pursue future studies of large-scale horizontal and vertical lithosphere motion in combination, as both of them track the expressions of past mantle flow. Such studies would provide powerful constraints for geodynamic inverse models of past mantle convection that are becoming feasible through the adjoint method.

Data accessibility. The oceanic spreading rates grid, the global plate motion model used to extract the spreading rates and the Base Hiatus Maps (BHS) have been previously published in Seton *et al.* [50], Müller *et al.* [27] and Hayek *et al.* [45,46], respectively.

Authors' contributions. B.V.: data curation, formal analysis, investigation, methodology, validation, visualization, writing—original draft, writing—review and editing; J.N.H.: data curation, formal analysis, investigation, methodology, validation, visualization, writing—original draft, writing—review and editing; I.L.S.: data curation, formal analysis, funding acquisition, investigation, methodology, validation, visualization, writing—original draft, writing—review and editing; H.-P.B.: conceptualization, formal analysis, funding acquisition, investigation, methodology, project administration, supervision, validation, writing—original draft, writing—review and editing; A.M.F.: conceptualization, investigation, methodology, supervision, validation; S.C.: data curation, formal analysis, investigation, methodology, validation; S.C.: investigation, methodology, supervision, validation, writing—review and editing.

All authors gave final approval for publication and agreed to be held accountable for the work performed therein.

Conflict of interest declaration. We declare we have no competing interests.

Funding. This research has been supported by the European Union's Horizon 2020 Research and Innovation Programme under the ERC-2019-STG project TEAR grant no. 852992 and the Deutsche Forschungsgemeinschaft project nos. STO1271/2-1 and BU2012/18-1.

Acknowledgements. We thank Dr Fred Richards, Prof. Nicholas Rawlinson and an anonymous reviewer for their thoughtful and constructive reviews. We appreciate their comments that improved the manuscript.

References

1. Richards MA, Lenardic A. 2018 The Cathles parameter (ct): a geodynamic definition of the asthenosphere and implications for the nature of plate tectonics. *Geochem. Geophys. Geosyst.* **19**, 4858–4875. (doi:10.1029/2018GC007821)
2. Barrell J. 1914 The strength of the Earth's crust. *J. Geol.* **22**, 655–683. (doi:10.1086/622181)
3. Chase CG. 1979 Asthenospheric counterflow: a kinematic model. *Geophys. J. Int.* **56**, 1–18. (doi:10.1111/j.1365-246X.1979.tb04764.x)

4. Hager BH, Richards MA. 1989 Long-wavelength variations in Earth's geoid: physical models and dynamical implications. *Phil. Trans. R. Soc. Lond. A* **328**, 309–327. (doi:10.1098/rsta.1989.0038)
5. Mitrovica JX. 1996 Haskell [1935] revisited. *J. Geophys. Res.: Solid Earth* **101**, 555–569. (doi:10.1029/95JB03208)
6. Bills BG, May GM. 1987 Lake Bonneville: constraints on lithospheric thickness and upper mantle viscosity from isostatic warping of Bonneville, Provo, and Gilbert stage shorelines. *J. Geophys. Res.: Solid Earth* **92**, 11 493–11 508. (doi:10.1029/JB092iB11p11493)
7. Wiens DA, Stein S. 1985 Implications of oceanic intraplate seismicity for plate stresses, driving forces and rheology. *Tectonophysics* **116**, 143–162. (doi:10.1016/0040-1951(85)90227-6)
8. Buck WR, Small C, Ryan WBF. 2009 Constraints on asthenospheric flow from the depths of oceanic spreading centers: the East Pacific Rise and the Australian-Antarctic Discordance. *Geochem. Geophys. Geosyst.* **10**, Q09007.
9. Debayle E, Kennett B, Priestley K. 2005 Global azimuthal seismic anisotropy and the unique plate-motion deformation of Australia. *Nature* **433**, 509–512. (doi:10.1038/nature03247)
10. Schaeffer AJ, Lebedev S, Becker TW. 2016 Azimuthal seismic anisotropy in the Earth's upper mantle and the thickness of tectonic plates. *Geophys. J. Int.* **207**, 901–933. (doi:10.1093/gji/ggw309)
11. Bunge HP, Richards MA. 1996 The origin of large scale structure in mantle convection: effects of plate motions and viscosity stratification. *Geophys. Res. Lett.* **23**, 2987–2990. (doi:10.1029/96GL02522)
12. Busse FH, Richards MA, Lenardic A. 2006 A simple model of high Prandtl and high Rayleigh number convection bounded by thin low-viscosity layers. *Geophys. J. Int.* **164**, 160–167. (doi:10.1111/j.1365-246X.2005.02836.x)
13. Tackley PJ. 1996 Effects of strongly variable viscosity on three-dimensional compressible convection in planetary mantles. *J. Geophys. Res.: Solid Earth* **101**, 3311–3332. (doi:10.1029/95JB03211)
14. Richards MA, Yang WS, Baumgardner JR, Bunge HP. 2001 Role of a low-viscosity zone in stabilizing plate tectonics: implications for comparative terrestrial planetology. *Geochem. Geophys. Geosyst.* **2**, 2000GC000115. (doi:10.1029/2000GC000115)
15. Morgan JP, Smith WH. 1992 Flattening of the sea-floor depth-age curve as a response to asthenospheric flow. *Nature* **359**, 524–527. (doi:10.1038/359524a0)
16. Morgan JP, Morgan WJ, Zhang YS, Smith WHF. 1995 Observational hints for a plume-fed, suboceanic asthenosphere and its role in mantle convection. *J. Geophys. Res.: Solid Earth* **100**, 12 753–12 767. (doi:10.1029/95JB00041)
17. Yamamoto M, Morgan JP, Morgan WJ. 2007 Global plume-fed asthenosphere flow-I: motivation and model development. In *Plates, plumes and planetary processes*, vol. 430 (eds GR Foulger, DM Jurdy), pp. 165–188. Boulder, CO: Geological Society of America.
18. Yamamoto M, Morgan JP, Morgan WJ. 2007 Global plume-fed asthenosphere flow-II: application to the geochemical segmentation of mid-ocean ridges. In *Plates, plumes and planetary processes*, vol. 430 (eds GR Foulger, DM Jurdy), pp. 189–208. Boulder, CO: Geological Society of America.
19. Höink T, Lenardic A. 2008 Three-dimensional mantle convection simulations with a low-viscosity asthenosphere and the relationship between heat flow and the horizontal length scale of convection. *Geophys. Res. Lett.* **35**, L10304. (10.1029/2008gl033854)
20. Höink T, Lenardic A. 2010 Long wavelength convection, Poiseuille-Couette flow in the low-viscosity asthenosphere and the strength of plate margins. *Geophys. J. Int.* **180**, 23–33. (doi:10.1111/j.1365-246X.2009.04404.x)
21. Höink T, Jellinek AM, Lenardic A. 2011 Viscous coupling at the lithosphere-asthenosphere boundary. *Geochem. Geophys. Geosyst.* **12**, Q0AK02. (doi:10.1029/2011gc003698)
22. Höink T, Lenardic A, Richards M. 2012 Depth-dependent viscosity and mantle stress amplification: implications for the role of the asthenosphere in maintaining plate tectonics. *Geophys. J. Int.* **191**, 30–41. (doi:10.1111/j.1365-246X.2012.05621.x)
23. Hager BH, Clayton RW, Richards MA, Comer RP, Dziewonski AM. 1985 Lower mantle heterogeneity, dynamic topography and the geoid. *Nature* **313**, 541–545. (doi:10.1038/313541a0)
24. Braun J. 2010 The many surface expressions of mantle dynamics. *Nat. Geosci.* **3**, 825–833. (doi:10.1038/ngeo1020)

25. DeMets C, Gordon RG, Argus DF. 2010 Geologically current plate motions. *Geophys. J. Int.* **181**, 1–80. (doi:10.1111/j.1365-246X.2009.04491.x)
26. Gordon RG, Jurdy DM. 1986 Cenozoic global plate motions. *J. Geophys. Res.: Solid Earth* **91**, 12 389–12 406. (doi:10.1029/JB091iB12p12389)
27. Müller RD*et al.* 2016 Ocean basin evolution and global-scale plate reorganization events since Pangea breakup. *Annu. Rev. Earth Planet. Sci.* **44**, 107–138. (doi:10.1146/annurev-earth-060115-012211)
28. Merkouriev S, DeMets C. 2014 High-resolution Neogene reconstructions of Eurasia-North America Plate motion. *Geophys. J. Int.* **198**, 366–384. (doi:10.1093/gji/ggu142)
29. DeMets C, Merkouriev S. 2019 High-resolution reconstructions of South America plate motion relative to Africa, Antarctica and North America: 34 Ma to present. *Geophys. J. Int.* **217**, 1821–1853. (doi:10.1093/gji/ggz087)
30. Iaffaldano G, Bodin T, Sambridge M. 2012 Reconstructing plate-motion changes in the presence of finite-rotations noise. *Nat. Commun.* **3**, 1048. (doi:10.1038/ncomms2051)
31. Iaffaldano G, Bunge H. 2009 Relating rapid plate-motion variations to plate-boundary forces in global coupled models of the mantle/lithosphere system: effects of topography and friction. *Tectonophysics* **474**, 393–404. (doi:10.1016/j.tecto.2008.10.035)
32. Colli L, Stotz I, Bunge HP, Smethurst M, Clark SR, Iaffaldano G, Tassara A, Guillocheau F, Bianchi MC. 2014 Rapid South Atlantic spreading changes and coeval vertical motion in surrounding continents: evidence for temporal changes of pressure-driven upper mantle flow. *Tectonics* **33**, 1304–1321. (doi:10.1002/2014TC003612)
33. Iaffaldano G, Bunge HP. 2015 Rapid plate motion variations through geological time: observations serving geodynamic interpretation. *Annu. Rev. Earth Planet. Sci.* **43**, 571–592. (doi:10.1146/annurev-earth-060614-105117)
34. Hoggard MJ, Winterbourne J, Czarnota K, White N. 2017 Oceanic residual depth measurements, the plate cooling model, and global dynamic topography. *J. Geophys. Res.: solid Earth* **122**, 2328–2372. (doi:10.1002/2016jb013457)
35. Fishwick S, Bastow ID. 2011 Towards a better understanding of African topography: a review of passive-source seismic studies of the African crust and upper mantle. *Geol. Soc. Lond. Spec. Publ.* **357**, 343–371. (doi:10.1144/SP357.19)
36. Ravenna M, Lebedev S, Fullea J, Adam JMC. 2018 Shear-wave velocity structure of southern Africa's lithosphere: variations in the thickness and composition of cratons and their effect on topography. *Geochem. Geophys. Geosyst.* **19**, 1499–1518. (doi:10.1029/2017GC007399)
37. Ernst RE, Buchan KL, eds. 2001 *Mantle plumes: their identification through time*, vol. 352. Boulder, CO: Geological Society of America.
38. Mitrovica JX, Beaumont C, Jarvis GT. 1989 Tilting of continental interiors by the dynamical effects of subduction. *Tectonics* **8**, 1079–1094. (doi:10.1029/TC008i005p01079)
39. Burgess PM, Gurnis M, Moresi L. 1997 Formation of sequences in the cratonic interior of North America by interaction between mantle, eustatic, and stratigraphic processes. *Geol. Soc. Am. Bull.* **109**, 1515–1535. (doi:10.1130/0016-7606(1997)109<1515:FOSITC>2.3.CO;2)
40. Miall AD. 2016 The valuation of unconformities. *Earth Sci. Rev.* **163**, 22–71. (doi:10.1016/j.earscirev.2016.09.011)
41. Friedrich AM, Bunge HP, Rieger SM, Colli L, Ghelichkhan S, Nerlich R. 2018 Stratigraphic framework for the plume mode of mantle convection and the analysis of interregional unconformities on geological maps. *Gondwana Res.* **53**, 159–188. (doi:10.1016/j.gr.2017.06.003)
42. Friedrich AM. 2019 Palaeogeological hiatus surface mapping: a tool to visualize vertical motion of the continents. *Geol. Mag.* **156**, 308–319. (doi:10.1017/S0016756818000560)
43. Vibe Y, Friedrich AM, Bunge HP, Clark SR. 2018 Correlations of oceanic spreading rates and hiatus surface area in the North Atlantic realm. *Lithosphere* **10**, 677–684. (doi:10.1130/L736.1)
44. Carena S, Bunge HP, Friedrich AM. 2019 Analysis of geological hiatus surfaces across Africa in the Cenozoic and implications for the timescales of convectively-maintained topography. *Can. J. Earth Sci.* **56**, 1333–1346. (doi:10.1139/cjes-2018-0329)
45. Hayek JN, Vilacís B, Bunge HP, Friedrich AM, Carena S, Vibe Y. 2020 Continent-scale Hiatus Maps for the Atlantic Realm and Australia since the Upper Jurassic and links to mantle flow induced dynamic topography. *Proc. R. Soc. A* **476**, 20200390. (doi:10.1098/rspa.2020.0390)
46. Hayek JN, Vilacís B, Bunge HP, Friedrich AM, Carena S, Vibe Y. 2021 Correction: continent-scale Hiatus Maps for the Atlantic Realm and Australia since the Upper Jurassic and links to mantle flow-induced dynamic topography. *Proc. R. Soc. A* **477**, 20210437. (doi:10.1098/rspa.2021.0437)

47. Cohen KM, Finney S, Gibbard PL, Fan JX. 2013 The ICS international chronostratigraphic chart. *Episodes* **36**, 199–204. Version 2018/08. (doi:10.18814/epiiugs/2013/v36i3/002)
48. Ogg JG, Ogg GM, Gradstein FM. 2016 1-Introduction. In *A concise geologic time scale* (eds JG Ogg, GM Ogg, FM Gradstein), pp. 1–8. Amsterdam, The Netherland: Elsevier.
49. Colli L, Ghelichkhan S, Bunge HP. 2016 On the ratio of dynamic topography and gravity anomalies in a dynamic Earth. *Geophys. Res. Lett.* **43**, 2510–2516. (doi:10.1002/2016GL067929)
50. Seton M, Müller RD, Zahirovic S, Williams S, Wright NM, Cannon J, Whittaker JM, Matthews KJ, McGirr R. 2020 A global data set of present-day oceanic crustal age and seafloor spreading parameters. *Geochem. Geophys. Geosyst.* **21**, e2020GC009214. (doi:10.1029/2020GC009214)
51. Ogg JG. 2012 Chapter 5—geomagnetic polarity time scale. In *The geologic time scale* (eds FM Gradstein, JG Ogg, MD Schmitz, GM Ogg), pp. 85–113. Boston, MA: Elsevier.
52. Müller RD*et al.* 2019 A global plate model including lithospheric deformation along major rifts and orogens since the Triassic. *Tectonics* **38**, 1884–1907. (doi:10.1029/2018TC005462)
53. Müller RD*et al.* 2018 GPlates: building a virtual Earth through deep time. *Geochem. Geophys. Geosyst.* **19**, 2243–2261. (doi:10.1029/2018GC007584)
54. Clark SR. 2018 Uncertainty in the breakup, spreading history, and velocity variations of Gondwana. *Gondwana Res.* **53**, 189–196. (doi:10.1016/j.gr.2017.04.029)
55. Seton M*et al.* 2012 Global continental and ocean basin reconstructions since 200 Ma. *Earth-Sci. Rev.* **113**, 212–270. (doi:10.1016/j.earscirev.2012.03.002)
56. Torsvik TH, Müller RD, Van der Voo R, Steinberger B, Gaina C. 2008 Global plate motion frames: toward a unified model. *Rev. Geophys.* **46**, RG3004. (doi:10.1029/2007RG000227)
57. Courtillot V, Davaille A, Besse J, Stock J. 2003 Three distinct types of hotspots in the Earth's mantle. *Earth Planet. Sci. Lett.* **205**, 295–308. (doi:10.1016/S0012-821X(02)01048-8)
58. Steinberger B, Torsvik TH. 2008 Absolute plate motions and true polar wander in the absence of hotspot tracks. *Nature* **452**, 620–623. (doi:10.1038/nature06824)
59. Levorsen AI. 1933 Studies in paleogeology. *AAPG Bull.* **17**, 1107–1132.
60. Stotz IL, Vilacís B, Hayek JN, Bunge HP, Friedrich AM. 2021 Yellowstone plume drives Neogene North American plate motion change. *Geophys. Res. Lett.* **48**, e2021GL095079. (doi:10.1029/2021GL095079)
61. Matthews KJ, Maloney KT, Zahirovic S, Williams SE, Seton M, Müller RD. 2016 Global plate boundary evolution and kinematics since the late Paleozoic. *Glob. Planet. Change.* **146**, 226–250. (doi:10.1016/j.gloplacha.2016.10.002)
62. Şengör AMC. 2001 Elevation as indicator of mantle-plume activity. In *Mantle plumes: their identification through time*, vol. 352 (eds RE Ernst, KL Buchan), pp. 183–245. Boulder, CO: Geological Society of America.
63. Davies GF, Richards MA. 1992 Mantle convection. *J. Geol.* **100**, 151–206. (doi:10.1086/629582)
64. Pitman W, Talwani M, Heirtzler J. 1971 Age of the North Atlantic Ocean from magnetic anomalies. *Earth Planet. Sci. Lett.* **11**, 195–200. (doi:10.1016/0012-821X(71)90163-4)
65. Gaina C, Roest W, Müller DR. 2002 Late Cretaceous-Cenozoic deformation of northeast Asia. *Earth Planet. Sci. Lett.* **197**, 273–286. (doi:10.1016/S0012-821X(02)00499-5)
66. Hillis RR*et al.* 2008 Cenozoic exhumation of the southern British Isles. *Geology* **36**, 371–374. (doi:10.1130/G24699A.1)
67. Japsen P, Green PF, Chalmers JA. 2005 Separation of Palaeogene and Neogene uplift on Nuussuaq, West Greenland. *J. Geol. Soc.* **162**, 299–314. (doi:10.1144/0016-764904-038)
68. Riis F. 1996 Quantification of Cenozoic vertical movements of Scandinavia by correlation of morphological surfaces with offshore data. *Glob. Planet. Change* **12**, 331–357. (doi:10.1016/0921-8181(95)00027-5)
69. von Eynatten H, Kley J, Dunkl I, Hoffmann VE, Simon A. 2021 Late Cretaceous to Paleogene exhumation in central Europe—localized inversion vs. large-scale domal uplift. *Solid Earth* **12**, 935–958. (doi:10.5194/se-12-935-2021)
70. Japsen P, Chalmers JA. 2000 Neogene uplift and tectonics around the North Atlantic: overview. *Glob. Planet. Change* **24**, 165–173. (doi:10.1016/S0921-8181(00)00006-0)
71. Stoker MS, Shannon PM. 2005 Neogene evolution of the NW European Atlantic margin: results from the STRATAGEM project. *Mar. Pet. Geol.* **22**, 965–968. (doi:10.1016/j.marpetgeo.2005.04.006)
72. Anell I, Thybom H, Artemieva IM. 2009 Cenozoic uplift and subsidence in the North Atlantic region: geological evidence revisited. *Tectonophysics* **474**, 78–105. TOPO-EUROPE: the geoscience of coupled deep Earth-surface processes. (doi:10.1016/j.tecto.2009.04.006)

73. Meco J, Scaillet S, Guillou H, Lomoschitz A, Carracedo JC, Ballester J, Betancort JF, Cilleros A. 2007 Evidence for long-term uplift on the Canary Islands from emergent Mio-Pliocene littoral deposits. *Glob. Planet. Change* **57**, 222–234. (doi:10.1016/j.gloplacha.2006.11.040)
74. Sehrt M, Glasmacher UA, Stockli DF, Jabour H, Kluth O. 2018 The southern Moroccan passive continental margin: an example of differentiated long-term landscape evolution in Gondwana. *Gondwana Res.* **53**, 129–144. (doi:10.1016/j.gr.2017.03.013)
75. Rickers F, Fichtner A, Trampert J. 2013 The Iceland-Jan Mayen plume system and its impact on mantle dynamics in the North Atlantic region: evidence from full-waveform inversion. *Earth Planet. Sci. Lett.* **367**, 39–51. (doi:10.1016/j.epsl.2013.02.022)
76. Celli NL, Lebedev S, Schaeffer AJ, Gaina C. 2021 The tilted Iceland Plume and its effect on the North Atlantic evolution and magmatism. *Earth Planet. Sci. Lett.* **569**, 117048. (doi:10.1016/j.epsl.2021.117048)
77. Poore HR, White N, Jones SM. 2009 A Neogene chronology of Iceland plume activity from V-shaped ridges. *Earth Planet. Sci. Lett.* **283**, 1–13. (doi:10.1016/j.epsl.2009.02.028)
78. Spice HE, Fitton JG, Kirstein LA. 2016 Temperature fluctuation of the Iceland mantle plume through time. *Geochem. Geophys. Geosyst.* **17**, 243–254. (doi:10.1002/2015GC006059)
79. Krob FC, Glasmacher UA, Bunge HP, Friedrich AM, Hackspacher PC. 2020 Application of stratigraphic frameworks and thermochronological data on the Mesozoic SW Gondwana intraplate environment to retrieve the Paraná-Etendeka plume movement. *Gondwana Res.* **84**, 81–110. (doi:10.1016/j.gr.2020.02.010)
80. Granot R, Dyment J. 2015 The cretaceous opening of the South Atlantic Ocean. *Earth Planet. Sci. Lett.* **414**, 156–163. (doi:10.1016/j.epsl.2015.01.015)
81. Guillocheau F, Rouby D, Robin C, Helm C, Rolland N, Le Carlier de Veslud C, Braun J. 2012 Quantification and causes of the terrigeneous sediment budget at the scale of a continental margin: a new method applied to the Namibia-South Africa margin. *Basin Res.* **24**, 3–30. (doi:10.1111/j.1365-2117.2011.00511.x)
82. Said A, Moder C, Clark S, Ghorbal B. 2015 Cretaceous-Cenozoic sedimentary budgets of the Southern Mozambique Basin: implications for uplift history of the South African Plateau. *J. Afr. Earth. Sci.* **109**, 1ï£¡ï£¡10. (doi:10.1016/j.jafrearsci.2015.05.007)
83. Baby G, Guillocheau F, Braun J, Robin C, Dall'Asta M. 2020 Solid sedimentation rates history of the Southern African continental margins: implications for the uplift history of the South African Plateau. *Terra Nova* **32**, 53–65. (doi:10.1111/ter.12435)
84. Jelsma H, Barnett W, Richards S, Lister G. 2009 Tectonic setting of kimberlites. *Lithos* **112**, 155–165. Proceedings of the 9th International Kimberlite Conference. (doi:10.1016/j.lithos.2009.06.030)
85. Paton DA, van der Spuy D, di Primio R, Horsfield B. 2008 Tectonically induced adjustment of passive-margin accommodation space; influence on the hydrocarbon potential of the Orange Basin, South Africa. *Am. Assoc. Pet. Geol. Bull.* **92**, 589–609. (doi:10.1306/12280707023)
86. Dressel I, Cacace M, Scheck-Wenderoth M. 2016 Coupled thermo-mechanical 3D subsidence analysis along the SW African passive continental margin. *Arab. J. Geosci.* **9**, 1–21. (doi:10.1007/s12517-016-2407-9)
87. Stanley JR, Flowers RM, Bell DR. 2015 Erosion patterns and mantle sources of topographic change across the southern African Plateau derived from the shallow and deep records of kimberlites. *Geochem. Geophys. Geosyst.* **16**, 3235–3256. (doi:10.1002/2015GC005969)
88. Green PF, Duddy IR, Japsen P, Bonow JM, Malan JA. 2015 Post-breakup burial and exhumation of the southern margin of Africa. *Basin Res.* **29**, 96–127. (doi:10.1111/bre.12167)
89. Storey M, Mahoney JJ, Saunders AD, Duncan RA, Kelley SP, Coffin MF. 1995 Timing of hot spot-related volcanism and the breakup of Madagascar and India. *Science* **267**, 852–855. (doi:10.1126/science.267.5199.852)
90. Torsvik TH, Tucker RD, Ashwal LD, Eide EA, Rakotosolofo NA, de Wit MJ. 1998 Late Cretaceous magmatism in Madagascar: palaeomagnetic evidence for a stationary Marion hotspot. *Earth Planet. Sci. Lett.* **164**, 221–232. (doi:10.1016/S0012-821X(98)00206-4)
91. Horton BK. 2018 Sedimentary record of Andean mountain building. *Earth Sci. Rev.* **178**, 279–309. (doi:10.1016/j.earscirev.2017.11.025)
92. Autin J*et al.* 2013 Colorado Basin 3D structure and evolution, Argentine passive margin. *Tectonophysics* **604**, 264–279. (doi:10.1016/j.tecto.2013.05.019)
93. Japsen P, Bonow JM, Green PF, Cobbold PR, Chiossi D, Lilletveit R, Magnavita LP, Pedreira A. 2012 Episodic burial and exhumation in NE Brazil after opening of the South Atlantic. *Bulletin* **124**, 800–816. (doi:10.1130/b30515.1)

94. Krob FC, Glasmacher UA, Karl M, Perner M, Hackspacher PC, Stockli DF. 2019 Multi-chronometer thermochronological modelling of the Late Neoproterozoic to recent *t-T*-evolution of the SE coastal region of Brazil. *J. South Am. Earth Sci.* **92**, 77–94. (doi:10.1016/j.jsames.2019.02.012)
95. Kollenz S, Glasmacher UA, Rossello EA, Stockli DF, Schad S, Pereyra RE. 2017 Thermochronological constraints on the Cambrian to recent geological evolution of the Argentina passive continental margin. *Tectonophysics* **716**, 182–203. (doi:10.1016/j.tecto.2016.11.019)
96. Sempere T, Folguera A, Gerbault M. 2008 New insights into Andean evolution: an introduction to contributions from the 6th ISAG symposium (Barcelona, 2005). *Tectonophysics* **459**, 1–13. (doi:10.1016/j.tecto.2008.03.011)
97. Rohde JK, Hoernle K, Hauff F, Werner R. 2013 Evidence for an age progression along the Tristan-Gough volcanic track from new $^{40}Ar/^{39}Ar$ ages on phenocryst phases. *Tectonophysics* **604**, 60–71. (doi:10.1016/j.tecto.2012.08.026)
98. Barker PF. 1983 Tectonic evolution and subsidence history of the Rio Grande Rise. In *1983 initial reports of the deep sea drilling project*, vol. 72 (eds PF Barker, RL Carlson, DA Johnson), pp. 953–976. Washington DC: US Government Printing Office.
99. MacGregor DS. 2013 Late Cretaceous–Cenozoic sediment and turbidite reservoir supply to South Atlantic margins. *Geol. Soc. Lond. Spec. Publ.* **369**, 109–128. (doi:10.1144/SP369.7)
100. Hall R. 2012 Late Jurassic-Cenozoic reconstructions of the Indonesian region and the Indian Ocean. *Tectonophysics* **570–571**, 1–41. (doi:10.1016/j.tecto.2012.04.021)
101. Harrington L, Zahirovic S, Salles T, Braz C, Müller RD. 2019 Tectonic, geodynamic and surface process driving forces of Australia's paleogeography since the Jurassic. In *The Sedimentary Basins of Western Australia V: Proc. of the Petroleum Exploration Society of Australia Symp., Perth, WA, 2019* (eds M Keep, S Moss), p. 29. Perth, Australia: Petroleum Exploration Society of Australia.
102. Sandiford M. 2007 The tilting continent: a new constraint on the dynamic topographic field from Australia. *Earth Planet. Sci. Lett.* **261**, 152–163. (doi:10.1016/j.epsl.2007.06.023)
103. DiCaprio L, Gurnis M, Müller RD. 2009 Long-wavelength tilting of the Australian continent since the Late Cretaceous. *Earth Planet. Sci. Lett.* **278**, 175–185. (doi:10.1016/j.epsl.2008.11.030)
104. Rosleff-Soerensen B, Reuning L, Back S, Kukla PA. 2016 The response of a basin-scale Miocene barrier reef system to long-term, strong subsidence on a passive continental margin, Barcoo Sub-basin, Australian North West Shelf. *Basin Res.* **28**, 103–123. (doi:10.1111/bre.12100)
105. Barnett-Moore N, Flament N, Heine C, Butterworth N, Müller RD. 2014 Cenozoic uplift of south Western Australia as constrained by river profiles. *Tectonophysics* **622**, 186–197. (doi:10.1016/j.tecto.2014.03.010)
106. Czarnota K, Roberts GG, White NJ, Fishwick S. 2014 Spatial and temporal patterns of Australian dynamic topography from River Profile Modeling. *J. Geophys. Res.: Solid Earth* **119**, 1384–1424. (doi:10.1002/2013JB010436)
107. Müller RD, Sdrolias M, Gaina C, Steinberger B, Heine C. 2008 Long-term sea-level fluctuations driven by ocean basin dynamics. *Science* **319**, 1357–1362. (doi:10.1126/.1151540)
108. Russell M, Gurnis M. 1994 The planform of epeirogeny: vertical motions of Australia during the Cretaceous. *Basin Res.* **6**, 63–76. (doi:10.1111/j.1365-2117.1994.tb00076.x)
109. Gurnis M. 1998 Cretaceous vertical motion of Australia and the Australian Antarctic discordance. *Science* **279**, 1499–1504. (doi:10.1126/science.279.5356.1499)
110. Storey BC. 1995 The role of mantle plumes in continental breakup: case histories from Gondwanaland. *Nature* **377**, 301–308. (doi:10.1038/377301a0)
111. Spasojevic S, Gurnis M, Sutherland R. 2010 Inferring mantle properties with an evolving dynamic model of the Antarctica-New Zealand region from the Late Cretaceous. *J. Geophys. Res.: Solid Earth* **115**, B05402.
112. Sutherland R, Spasojevic S, Gurnis M. 2010 Mantle upwelling after Gondwana subduction death explains anomalous topography and subsidence histories of eastern New Zealand and West Antarctica. *Geology* **38**, 155–158. (doi:10.1130/G30613.1)
113. Hoernle K*et al.* 2020 Late Cretaceous (99-69 Ma) basaltic intraplate volcanism on and around Zealandia: tracing upper mantle geodynamics from Hikurangi Plateau collision to Gondwana breakup and beyond. *Earth Planet. Sci. Lett.* **529**, 115864. (doi:10.1016/j.epsl.2019.115864)

114. Stotz IL, Tassara A, Iaffaldano G. 2021 Pressure-driven Poiseuille flow inherited from Mesozoic mantle circulation led to the Eocene separation of Australia and Antarctica. *J. Geophys. Res.: Solid Earth* **126**, e2020JB019945. (doi:10.1029/2020JB019945)
115. Warners-Ruckstuhl KN, Meijer PT, Govers R, Wortel MJ. 2010 A lithosphere-dynamics constraint on mantle flow: analysis of the Eurasian plate. *Geophys. Res. Lett.* **37**, L18308. (doi:10.1029/2010GL044431)
116. Warners-Ruckstuhl KN, Govers R, Wortel R. 2012 Lithosphere-mantle coupling and the dynamics of the Eurasian Plate. *Geophys. J. Int.* **189**, 1253–1276. (doi:10.1111/j.1365-246X.2012.05427.x)
117. Copley A, Avouac JP, Royer JY. 2010 India-Asia collision and the Cenozoic slowdown of the Indian plate: implications for the forces driving plate motions. *J. Geophys. Res.: Solid Earth* **115**, B03410. (doi:10.1029/2009JB006634)
118. Warners-Ruckstuhl KN, Govers R, Wortel R. 2013 Tethyan collision forces and the stress field of the Eurasian Plate. *Geophys. J. Int.* **195**, 1–15. (doi:10.1093/gji/ggt219)
119. Iaffaldano G, Davies DR, Demets C. 2018 Indian Ocean floor deformation induced by the Reunion plume rather than the Tibetan Plateau. *Nat. Geosci.* **11**, 362–366. (doi:10.1038/s41561-018-0110-z)
120. Iaffaldano G. 2021 Has the Tibetan Plateau risen in the Early/Mid-Miocene? Constraints from plate-motion reconstructions and seismicity of the Indian Ocean lithosphere. *Geophys. J. Int.* **225**, 1349–1358. (doi:10.1093/gji/ggab027)
121. Ehlers TA, Farley KA. 2003 Apatite (U–Th)/He thermochronometry: methods and applications to problems in tectonic and surface processes. *Earth Planet. Sci. Lett.* **206**, 1–14. (doi:10.1016/S0012-821X(02)01069-5)
122. Kohn MJ, ed. 2007 *Paleoaltimetry: geochemical and thermodynamic approaches*, vol. 66. Reviews in Mineralogy and Geochemistry. Virgina: De Gruyter.
123. Roberts GG, White N. 2010 Estimating uplift rate histories from river profiles using African examples. *J. Geophys. Res.: Solid Earth* **115**, B02406. (doi:10.1029/2009jb006692)
124. Guillocheau F, Simon B, Baby G, Bessin P, Robin C, Dauteuil O. 2018 Planation surfaces as a record of mantle dynamics: the case example of Africa. *Gondwana Res.* **53**, 82–98. (doi:10.1016/j.gr.2017.05.015)
125. Meinhold G. 2010 Rutile and its applications in Earth sciences. *Earth-Sci. Rev.* **102**, 1–28. (doi:10.1016/j.earscirev.2010.06.001)
126. Flowers R, Wernicke B, Farley K. 2008 Unroofing, incision, and uplift history of the southwestern Colorado Plateau from apatite (U-Th)/He thermochronometry. *GSA Bull.* **120**, 571–587. (doi:10.1130/B26231.1)
127. Reiners PW, Brandon MT. 2006 Using thermochronology to understand orogenic erosion. *Annu. Rev. Earth Planet. Sci.* **34**, 419–466. (doi:10.1146/annurev.earth.34.031405.125202)
128. Hodges K. 2003 3.08—Geochronology and thermochronology in orogenic systems. In *Treatise on geochemistry* (eds HD Holland, KK Turekian), pp. 263–292. Oxford, UK: Pergamon.
129. Fernandes VM, Roberts GG. 2020 Cretaceous to Recent net continental uplift from paleobiological data: insights into sub-plate support. *GSA Bull.* **133**, 1217–1236. (doi:10.1130/B35739.1)
130. Said A, Moder C, Clark S, Abdelmalak MM. 2015 Sedimentary budgets of the Tanzania coastal basin and implications for uplift history of the East African rift system. *J. Afr. Earth. Sci.* **111**, 288–295. (doi:10.1016/j.jafrearsci.2015.08.012)
131. Hoggard MJ, Austerman J, Randel C, Stephenson S. 2021 Observational estimates of dynamic topography through space and time. In *Mantle convection and surface expressions* (eds H Marquardt, M Ballmer, S Cottaar, J Konter), ch. 15, pp. 371–411. Washington DC: American Geophysical Union (AGU).
132. Campbell IH, Griffiths RW. 1990 Implications of mantle plume structure for the evolution of flood basalts. *Earth Planet. Sci. Lett.* **99**, 79–93. (doi:10.1016/0012-821X(90)90072-6)
133. Farnetani CG, Richards MA. 1994 Numerical investigations of the mantle plume initiation model for flood basalt events. *J. Geophys. Res.* **99**, 13 813–13 833. (doi:10.1029/94JB00649)
134. Campbell IH. 2007 Testing the plume theory. *Chem. Geol.* **241**, 153–176. (doi:10.1016/j.chemgeo.2007.01.024)
135. Stotz IL, Iaffaldano G, Davies DR. 2018 Pressure-driven Poiseuille flow: a major component of the torque-balance governing Pacific plate motion. *Geophys. Res. Lett.* **45**, 117–125. (doi:10.1002/2017GL075697)

136. Paulson A, Richards MA. 2009 On the resolution of radial viscosity structure in modelling long-wavelength postglacial rebound data. *Geophys. J. Int.* **179**, 1516–1526. (doi:10.1111/j.1365-246X.2009.04362.x)
137. Hartley RA, Roberts GG, White N, Richardson C. 2011 Transient convective uplift of an ancient buried landscape. *Nat. Geosci.* **4**, 562–565. (doi:10.1038/ngeo1191)
138. Weismüller J, Gmeiner B, Ghelichkhan S, Huber M, John L, Wohlmuth B, Rüde U, Bunge HP. 2015 Fast asthenosphere motion in high-resolution global mantle flow models. *Geophys. Res. Lett.* **42**, 7429–7435. (doi:10.1002/2015GL063727)
139. Steinberger B, Schmeling H, Marquart G. 2001 Large-scale lithospheric stress field and topography induced by global mantle circulation. *Earth Planet. Sci. Lett.* **186**, 75–91. (doi:10.1016/S0012-821X(01)00229-1)
140. Kendall JM, Lithgow-Bertelloni C. 2016 Why is Africa rifting? *Geol. Soc. Lond. Spec. Publ.* **420**, 11–30. (doi:10.1144/SP420.17)
141. Bird P, Liu Z, Rucker WK. 2008 Stresses that drive the plates from below: definitions, computational path, model optimization, and error analytsis. *J. Geophys. Res.* **113**, B11406. (doi:10.1029/2007JB005460)
142. Colli L, Ghelichkhan S, Bunge HP, Oeser J. 2018 Retrodictions of Mid Paleogene mantle flow and dynamic topography in the Atlantic region from compressible high resolution adjoint mantle convection models: sensitivity to deep mantle viscosity and tomographic input model. *Gondwana Res.* **53**, 252–272. (doi:10.1016/j.gr.2017.04.027)
143. Ghelichkhan S, Bunge HP, Oeser J. 2021 Global mantle flow retrodictions for the early Cenozoic using an adjoint method: evolving dynamic topographies, deep mantle structures, flow trajectories and sublithospheric stresses. *Geophys. J. Int.* **226**, 1432–1460. (doi:10.1093/gji/ggab108)
144. Harper JF. 1975 On the driving forces of plate tectonics. *Geophys. J. Int.* **40**, 465–474. (doi:10.1111/j.1365-246X.1975.tb04143.x)
145. Westaway R. 1993 Forces associated with mantle plumes. *Earth Planet. Sci. Lett.* **119**, 331–348. (doi:10.1016/0012-821X(93)90142-V)
146. Van Hinsbergen DJ, Steinberger B, Doubrovine PV, Gassmöller R. 2011 Acceleration and deceleration of India-Asia convergence since the Cretaceous: roles of mantle plumes and continental collision. *J. Geophys. Res.: Solid Earth* **116**, B06101. (doi:10.1029/2010JB008051)
147. Cande SC, Stegman DR. 2011 Indian and African plate motions driven by the push force of the Réunion plume head. *Nature* **475**, 47–52. (doi:10.1038/nature10174)
148. Karato S, Wu P. 1993 Rheology of the upper mantle: a synthesis. *Science* **260**, 771–778. (doi:10.1126/science.260.5109.771)
149. Semple AG, Lenardic A. 2018 Plug flow in the Earth's asthenosphere. *Earth Planet. Sci. Lett.* **496**, 29–36. (doi:10.1016/j.epsl.2018.05.030)
150. Parnell-Turner R, White N, Henstock T, Murton B, Maclennan J, Jones SM. 2014 A continuous 55-million-year record of transient mantle plume activity beneath Iceland. *Nat. Geosci.* **7**, 914–919. (doi:10.1038/ngeo2281)
151. O'Neill C, Müller RD, Steinberger B. 2005 On the uncertainties in hot spot reconstructions and the significance of moving hot spot reference frames. *Geochem. Geophys. Geosyst.* **6**, Q04003. (doi:10.1029/2004GC000784)
152. Steinberger B, O'Connell RJ. 1997 Changes of the Earth's rotation axis owing to advection of mantle density heterogeneities. *Nature* **387**, 169–173. (doi:10.1038/387169a0)
153. Shephard GE, Bunge HP, Schuberth BS, Müller RD, Talsma A, Moder C, Landgrebe T. 2012 Testing absolute plate reference frames and the implications for the generation of geodynamic mantle heterogeneity structure. *Earth Planet. Sci. Lett.* **317**, 204–217. (doi:10.1016/j.epsl.2011.11.027)
154. Becker TW, Schaeffer AJ, Lebedev S, Conrad CP. 2015 Toward a generalized plate motion reference frame. *Geophys. Res. Lett.* **42**, 3188–3196. (doi:10.1002/2015GL063695)
155. Müller RD, Royer JY, Lawver LA. 1993 Revised plate motions relative to the hotspots from combined Atlantic and Indian Ocean hotspot tracks. *Geology* **21**, 275–278. (doi:10.1130/0091-7613(1993)021<0275:RPMRTT>2.3.CO;2)
156. Bunge HP. 2005 Low plume excess temperature and high core heat flux inferred from non-adiabatic geotherms in internally heated mantle circulation models. *Phys. Earth Planet. Inter.* **153**, 3–10. (doi:10.1016/j.pepi.2005.03.017)
157. Simmons NA, Forte AM, Grand SP. 2009 Joint seismic, geodynamic and mineral physical constraints on three-dimensional mantle heterogeneity: implications for the relative

importance of thermal versus compositional heterogeneity. *Geophys. J. Int.* **177**, 1284–1304. (doi:10.1111/j.1365-246X.2009.04133.x)
158. Davies JH, Davies DR. 2010 Earth's surface heat flux. *Solid Earth* **1**, 5–24. (doi:10.5194/se-1-5-2010)
159. Gordon RG. 2009 Lithospheric deformation in the equatorial Indian Ocean: timing and Tibet. *Geology* **37**, 287–288. (doi:10.1130/focus032009.1)
160. Iaffaldano G, Husson L, Bunge HP. 2011 Monsoon speeds up Indian plate motion. *Earth Planet. Sci. Lett.* **304**, 503–510. (doi:10.1016/j.epsl.2011.02.026)
161. Coltice N, Shephard GE. 2018 Tectonic predictions with mantle convection models. *Geophys. J. Int.* **213**, 16–29. (doi:10.1093/gji/ggx531)